



Mercury's Lobate Scarps Reveal that Polygonal Impact Craters Form on Contractional Structures

Chloe B. Beddingfield¹ , Kelsey Crane² , Christian Klimczak³ , and Richard Cartwright¹

¹ Johns Hopkins University Applied Physics Laboratory, MD, USA; chloe.beddingfield@jhuapl.edu

² Mississippi State University, Starkville, MS, USA

³ University of Georgia, Athens, GA, USA

Received 2023 November 5; revised 2024 January 9; accepted 2024 January 16; published 2024 February 27

Abstract

Analysis of polygonal impact craters (PICs) can be used to investigate the presence and orientations of subtle and/or buried faults and fractures across the solar system that may otherwise be unobservable in spacecraft images. Although this technique has been vetted for the analysis of extensional structures, no previous work has investigated if PICs also form on contractional thrust faults. This determination, which we investigated in this work, is critical for accurate tectonic setting interpretations from PICs. Mercury shows an abundance of thrust-fault-related landforms, making it an ideal laboratory to perform this investigation. In this work, we found that Mercury's thrust faults, and their overlying folds and fractures, cause some complex craters ~20 km or larger to form PICs. However, in most cases, craters form as circular impact craters on these structures. When PIC straight rim segments do form, they parallel the lobate scarp thrust faults and fold hinges. Some PICs likely formed as a result of an impact's interaction with the thrust fault itself, while others may have interacted with fold hinge joints. The parallel relationship between PICs and shortening structures is consistent with the well-established relationship between PICs and extensional structures. Therefore, in addition to extensional fractures, contractional features should also be taken into consideration when utilizing PICs to interpret tectonic settings on bodies across the solar system.

Unified Astronomy Thesaurus concepts: Planetary science (1255); Mercury (planet) (1024); Tectonics (2175); Impact phenomena (779); Craters (2282)

1. Introduction

Polygonal impact craters (PICs), craters with one or more straight edges along their rims, have been identified on planetary bodies across the solar system (Figure 1) and form when an impact event occurs in a target with preexisting faults or fractures (Fielder 1961; Shoemaker 1962, 1963; Roddy 1978; Öhman et al. 2005; Beddingfield et al. 2016; Beddingfield & Cartwright 2020). Because PIC straight rim segments in many cases align with subimage resolution and/or subregolith fracture systems, they can provide crucial information for deciphering the tectonic histories of planetary bodies. For example, PICs have been used to more completely infer global-scale deformation patterns on the Saturnian moons Iapetus (Singer & McKinnon 2011) and Dione (e.g., Beddingfield et al. 2016) and the Uranian moon Miranda (Beddingfield & Cartwright 2020). However, only the association and relationship between PICs and extensional tectonic structures have been previously established. The association of PICs with contractional tectonic landforms has not been investigated on any planetary body or by utilizing physical models. Therefore, the interpretation of global-scale deformation patterns inferred from PICs is limited by the lack of knowledge regarding the possible association and orientation relationship between PICs and faults that accommodates lithospheric shortening.

Mercury is known to exhibit PICs (e.g., Weihs et al. 2015), as well as craters superposed on shortening landforms, so-called lobate scarps and wrinkle ridges (e.g., Banks et al. 2015;

Crane & Klimczak 2017). Both of these landform types are widely accepted to be the surface expressions of combinations of thrust faults and folds (Strom et al. 1975; Cordell & Strom 1977; Melosh & McKinnon 1988; Watters et al. 1998, 2001, 2004). Their formation is widely attributed to global contraction, the process causing Mercury to shrink from the long, sustained cooling of the planet (e.g., McKinnon 2014; Byrne 2018). Extensional landforms such as normal faults and graben are also curiously absent on Mercury's surface aside from those observed within plains units inside basins (Watters et al. 2009a, 2009b; Blair et al. 2013). Therefore, Mercury's surface represents an ideal test bed to investigate how impact cratering processes interact with preexisting contractional structures. In this work, we investigated if there is a relationship between PICs and lobate scarps to gain invaluable insight into how contractional structures affect crater morphologies.

Furthermore, the origin of PICs across the surface of Mercury remains uncertain because a general relationship between thrust faults and PICs has not been determined. Quantifying this relationship is therefore needed to use PICs as a tool to investigate Mercury's tectonic history. Detection and characterization of the orientations of subtle fracture systems would help discriminate between different tectonic processes on the innermost planet. For example, tidal despinning—the slowing of rotation to lock Mercury in its current 3:2 spin-orbit resonance with the Sun—is proposed to have formed a global fracture pattern (Klimczak et al. 2015); however, structural artifacts from this event and other early processes were likely overprinted by shortening landforms driven by global contraction, the volumetric reduction of Mercury due to long, sustained planetary cooling (Solomon 1977). Overprinting would have included the reactivation of favorably oriented



Original content from this work may be used under the terms of the [Creative Commons Attribution 4.0 licence](#). Any further distribution of this work must maintain attribution to the author(s) and the title of the work, journal citation and DOI.

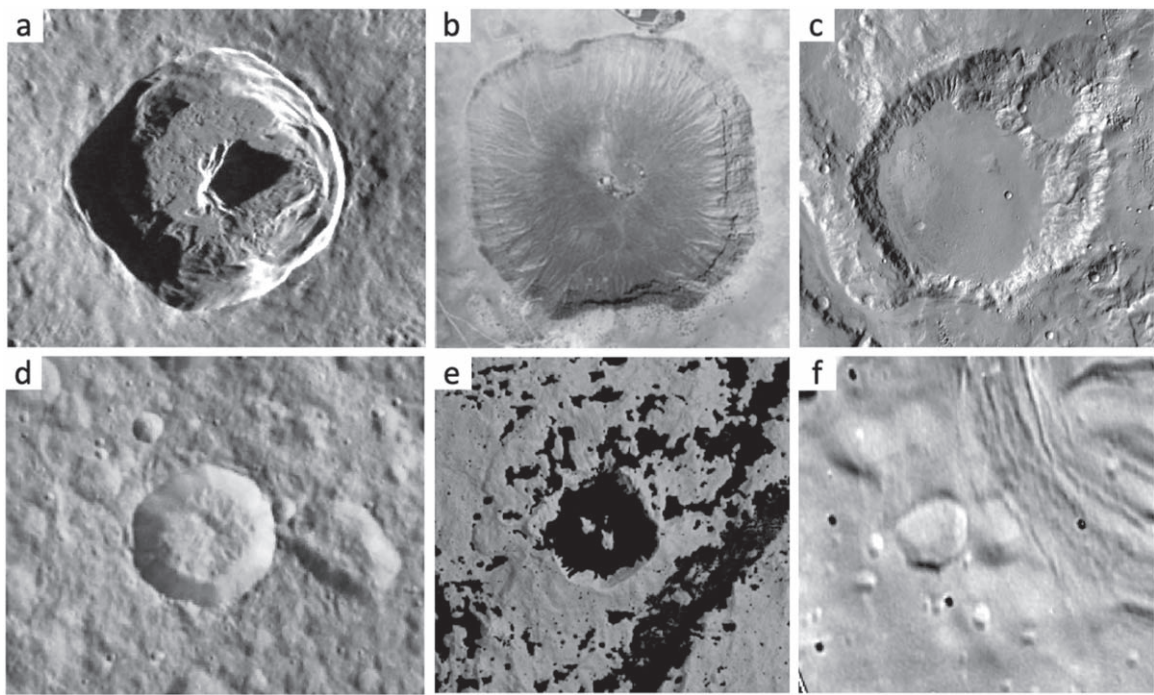


Figure 1. Examples of PICs on rocky and icy bodies across the solar system. (a) Mercury: Cunningham Crater ($D = 37$ km; coordinates: $30^{\circ}38'5$, $157^{\circ}13'$), a PIC identified in this study within Caloris Basin. This figure shows a portion of MDIS image EW0220375119G. (b) Earth: Barringer (Meteor) Crater ($D = 1.2$ km; coordinates: $35^{\circ}03'$, $111^{\circ}02'$) in Arizona. This figure panel is a modified version of Figure 1(b) from Kumar & Kring (2008). (c) Mars: Martynov Crater, a PIC ($D = 61$ km; coordinates: $323^{\circ}6$, $-30^{\circ}4$) identified by Öhman et al. (2006), located north of the Argyre basin. (d) Dione: a PIC ($D = 27$ km; coordinates: $20^{\circ}1$, $213^{\circ}4$) identified by Beddingfield et al. (2016) within the Wispy Terrain. (e) Iapetus: a PIC ($D = 21$ km; coordinates: -7° , 114°) identified by Singer & McKinnon (2011). (f) Miranda: a PIC ($D = 11$ km; coordinates: $-36^{\circ}4$, $225^{\circ}2$) identified by Beddingfield & Cartwright (2020), located in the cratered terrain near Elsinore Corona.

fracture sets (Klimczak et al. 2015) but not the destruction of those unfavorably oriented. Those sets remain hidden but could be expressed during PIC formation. Therefore, characterization of PICs provides insight into how other tectonic processes, along with global contraction, played a role in shaping the surface of Mercury.

2. Background

2.1. Controls on Impact Crater Morphologies

Differences in impactor and target material properties influence the resulting impact crater morphologies. For a given impactor and impact velocity, the diameter of an impact crater will be larger on planets and satellites with lower gravity and lower target material density (e.g., De Pater & Lissauer 2010). Higher-velocity impacts will form craters with larger diameters, as will an increase in the density or size of the impactor. Impact crater geometries depend on other factors, including the angle of impact (e.g., Herrick & Forsberg-Taylor 2003), whether or not impacts are clustered (e.g., O’Keefe & Ahrens 1982; Schultz & Gault 1985b; Cochrane & Ghail 2006), the topography of the target area (e.g., Gifford & Maxwell 1979), the layering of the target material (Quaide & Oberbeck 1968), erosion (Ronca & Salisbury 1966), postimpact tectonic modification (e.g., Pappalardo & Collins 2005; Watters & Johnson 2010), and the presence of preexisting subvertical structures within the target material (e.g., Eppler et al. 1983; Kumar & Kring 2008). In addition to target material properties, crater geometries may also be affected by properties of the projectile including the porosity, composition, and shape (e.g., Schultz & Gault 1985a; Melosh 1989; Osinski & Pierazzo 2013).

Circular impact craters (CICs) are inferred to result from impact events in target material with uniform,

multidirectional strength properties (e.g., Melosh 1989). This material could be nontectonized and so uniformly strong, or prefRACTURED, if the fractures are widely or closely spaced relative to the size of the resulting crater (e.g., Fulmer & Roberts 1963). Additionally, CICs can form in a fractured target if the fracture system is highly complex or covered by a thick layer of noncohesive sediment that limits interactions between the impactor and the underlying bedrock (e.g., Fulmer & Roberts 1963). In contrast, the only known cause for the formation of PICs is the presence of preexisting subvertical structures within the target material (e.g., Fielder 1965; Eppler et al. 1983; Öhman et al. 2005, 2008; Öhman 2009; Aittola et al. 2010). PICs exhibit straight rim segments, which reflect the orientations of preexisting fractures in the target material (e.g., Fielder 1961; Shoemaker 1962, 1963; Roddy 1978; Öhman et al. 2005). Consequently, CICs and PICs are excellent tools to distinguish between nontectonized and tectonized terrains on the surfaces of both silicate-rich and ice-rich surfaces across the solar system (e.g., Öhman et al. 2006; Beddingfield et al. 2016; Beddingfield & Cartwright 2020; Robbins & Riggs 2023).

2.2. Models of PIC Formation in Extensional Settings

Four PIC formation models have been investigated previously, each requiring the target material to contain preexisting fractures, which we refer to as models A, B, C, and D. Descriptions of these models are provided in detail by Öhman (2009), so we only summarize them here. According to model A, simple PICs are structurally controlled during the excavation stage of the transient crater (e.g., Schultz 1976; Eppler et al. 1983). The cavity expands in a direction oriented 45° to the surrounding fracture azimuths, forming PICs with azimuths that are offset by

45° to azimuths of the controlling fractures. This model is based on observations of two orthogonal fracture sets trending 45° to the straight crater rim segments of Barringer (Meteor) Crater located near Flagstaff, Arizona (Shoemaker 1963, 1977; Gault et al. 1974; Schultz 1976; Roddy 1978; Poelchau et al. 2008, 2009).

In model B, simple PIC shapes form as excavation flow preferentially overturns material along preexisting fractures, causing the crater to preferentially expand perpendicular to the fracture azimuths. In this model, the final PIC azimuths parallel surrounding fracture azimuths (Kumar & Kring 2008).

In model C, complex PIC geometries are determined during the modification stage (e.g., Schultz 1976; Eppler et al. 1983). In this model, the crater's straight rim segments are a result of the transient crater walls slumping via modification-related normal faulting along preexisting target structures along the crater wall. Consequently, the crater expands in a direction parallel to surrounding fracture azimuths. Like model B for simple PICs, this activity results in a parallel PIC–fracture relationship for complex craters.

In model D, applicable to both simple and complex craters, PICs inherit their geometries from movement of material along preexisting structures during the excavation stage (Öhman 2009). Like models B and C, model D predicts that the final PIC azimuths parallel surrounding fracture azimuths. Model D is supported by observational evidence of an association between faults and PIC crater rims on planetary surfaces (e.g., Gault et al. 1974; Reimold et al. 1998).

2.3. PICs throughout the Solar System

PICs have been identified throughout the solar system, and the relationships between PIC straight rim segment azimuths and controlling fracture azimuths have been investigated on many planetary bodies (e.g., Öhman 2009; Öhman et al. 2010). PICs are abundant on solid surfaces, and methods of automated detection of crater geometries are under investigation (Robbins & Riggs 2023). PIC azimuths on Mercury (Melosh & Dzurisin 1978; Strom & Sprague 2003) and Venus (Aittola et al. 2007, 2008, 2010; Öhman 2009) have been found to parallel azimuths of surrounding linear structures. On Earth, many PICs have also been identified, and their orientations have been compared to those of surrounding structures for both simple craters (e.g., Öhman 2009) and complex craters (e.g., Morrison 1984).

PICs have been used to infer global-scale deformation patterns on the Saturnian moons Iapetus (Singer & McKinnon 2011) and Dione (Beddingfield et al. 2016) and on the Uranian moon Miranda (Beddingfield & Cartwright 2020). Additionally, PICs have been investigated on Ceres (Zeilhofer & Barlow 2021). Some PICs on Miranda overprint a terrain that has been interpreted to be made up of either contractional tectonic structures or cryovolcanically formed ridges (Schenk 1991; Beddingfield & Cartwright 2020). Earth's Moon also exhibits PICs (e.g., Fulmer & Roberts 1963; Melosh 1976; Schultz 1976; Eppler et al. 1983), and their azimuths parallel those of surrounding fractures (e.g., Melosh 1976; Schultz 1976; Eppler et al. 1983). Similarly, Martian PICs have been associated with the presence of preexisting target structures (Thomas & Allemand 1993; Watters 2006, 2009). PICs are also present on the surfaces of asteroids (Belton et al. 1994; Veverka et al. 1997; Thomas et al. 1999; Zuber et al. 2000; Pockert et al. 2002), the nucleus of a comet (Basilevsky & Keller 2006), and several other icy satellites (Smith et al. 1981; Plescia 1983; Porco et al. 2005; Helfenstein et al. 2005;

Beddingfield et al. 2016, 2020). See Robbins & Riggs (2023) for a recent detailed summary of PICs identified throughout the solar system.

2.4. PICs on Mercury in a Contractional Tectonic Setting

Mercury exhibits PICs on its surface (Figure 1(a)) that were first systematically documented by Herrick et al. (2011) in the production of a global catalog of Mercurian craters. Weihs et al. (2015) visually inspected craters in this catalog and marked those with at least two straight rim segments as being polygonal, with 33 of the 291 assessed craters meeting this criterion. A recent study of PICs on Mercury systematically mapped and analyzed over 7000 impact craters, finding nearly 29,000 straight rim segments longer than 10 km (Yazici & Klimczak 2021; Yazici et al. 2024). These authors found that, in contrast to previous work that estimated PICs to represent ~11% of craters on Mercury (Weihs et al. 2015), 83% of craters in their study contained straight rim segments. Both studies noticed roughly east–west orientations in straight rim segments near the poles; however, Yazici et al. (2024) also noted a weak preference for north–south orientations closer to the equator. Both studies located a range of sizes for PICs, 20–400 km (Yazici et al. 2024) and 65–240 km (Weihs et al. 2015).

Because PICs utilize preexisting fractures during their formation, the orientations of PIC walls in the spatial context of lobate scarps would inform our understanding of how folding progresses on Mercury. PIC straight rim segments aligned with the orientation of shortening landforms could indicate that pure shear accommodates folding and that folding and fracturing are coincident. Alternatively, PIC walls oriented obliquely to the fold hinge could be used to infer prefolding stress directions that may have generated tectonic fabrics prior to folding. It is also possible that both scenarios exist, and thus fracturing both before and during folding could be evaluated. The spatial density of PICs with along-trend versus oblique-to-trend walls could be evaluated to determine the spatial variability in tectonic fabric and shear strain. It is widely anticipated that many fracturing processes, unrelated to lobate scarp formation, occurred globally and regionally across Mercury's surface. Stresses resulting in these fractures may have been derived from tidal despinning (Klimczak et al. 2015), polar wander due to the Caloris Basin mascon (Matsuyama & Nimmo 2009), mantle upwelling or downwelling (King 2008; Tosi et al. 2013), or any combination of these processes over time. If sufficient in magnitude, stresses from these processes also would have produced fractures that resulted in PIC formation.

All models of PIC formation emphasize the necessity of subvertical fractures, regardless of their orientations. For lobate scarps, underlying major fault structures are predicted to dip between 5° (Galluzzi et al. 2019; Crane 2020) and 45° (Galluzzi et al. 2015; Watters 2021) on Mercury, with the theory of faulting predicting thrust faults to have optimal dips of 30° (Anderson 1951; Jaeger et al. 2009). The often rounded, asymmetric surface expressions of lobate scarps imply anticlinal folding above the underlying thrust faults. These folds on Earth are observed to contain fracture sets in various orientations relative to their limbs and hinges—not all of which are shallowly dipping (Figure 2; also see Figure 11 in Klimczak et al. 2019). Extension in the outer hinges causes near vertical shear fractures and jointing in these outer layers and shallowly dipping conjugate fracture sets in the inner hinges (Ramsay 1967; Cosgrove 2015). These joints may be accompanied by additional

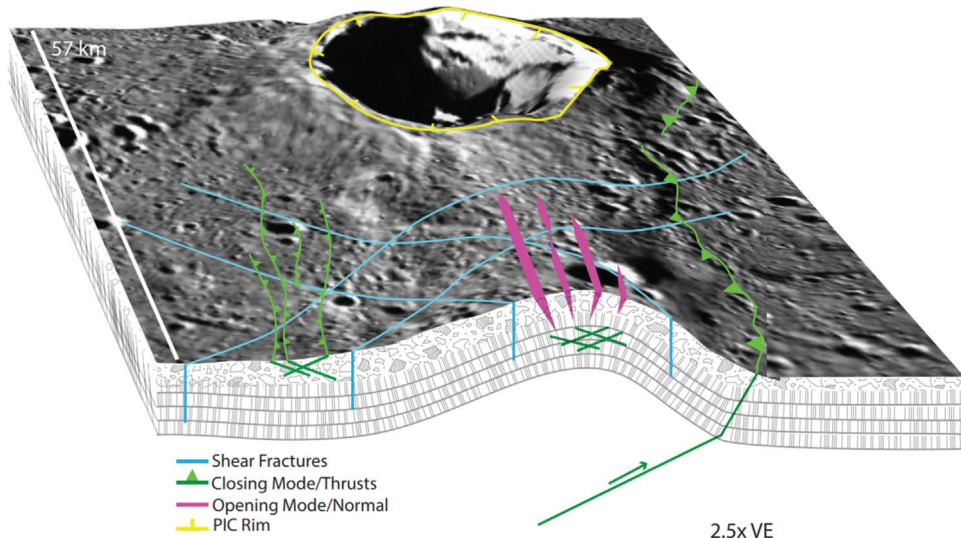


Figure 2. Examples of anticline fractures that may result from folding above thrust faults on Mercury.

fractures caused by regional tectonic stresses, flexural slip, and intraunit stresses. Conjugate joint sets steeply dipping with orientations 60° from the hinge orientation may occur (Price & Cosgrove 1990) as well as nearly vertical joints perpendicular to the hinge (Reber et al. 2010), which may result from buckling (Eckert et al. 2014). Thus, horizontal compression and shortening, especially when in association with folding, do not limit the presence of steep fracture networks.

Although Mercury's lobate scarps form from strong, horizontally compressive stresses, the crests of these landforms often display graben or opening mode fractures, signs of outer-arc extension, localized within the fold hinge (Byrne et al. 2018; Klimczak et al. 2019; Man et al. 2023). Where these fractures align with the overall trend of the landform, it may be interpreted that pure shear has dominated the strain history causing fracturing during folding (Ramsey 1968). However, fractures can also be observed crossing the hinge zone obliquely (Figure 2), implying that fractures accommodate regional stresses prior to folding (e.g., Ahmadhadi et al. 2008).

3. Data and Methods

We identified and investigated PICs on Mercury's lobate scarps by using a series of statistical tests. We utilized the R language to analyze rim azimuth distributions for each crater investigated. The steps discussed below are provided in additional detail in previous PIC studies (Beddingfield et al. 2016; Beddingfield & Cartwright 2020). For an overview of all steps outlined in the following subsections, see the flowchart in Figure 3. Due to the large number of craters analyzed in this study, the Appendix contains much of the information on crater and image data (Table A1), identified PICs (Figures A1–A3), statistical test information (Table A2), collected azimuth data for PICs and lobate scarps (Figures A4–A9), descriptions of lobate scarp proximities to craters (Table A3), and lobate scarp dip directions (Table A4).

3.1. Crater Selection Criteria

We assessed the craters identified by Crane & Klimczak (2017) that are in overprinting stratigraphic relationships with lobate scarps. As summarized in Crane & Klimczak (2017), craters that are superposed by faults and those that overprint

faults were distinguished. These identified craters are based on the thrust-fault-related data set provided by Byrne et al. (2014) and the Kinczyk et al. (2020) data set of craters with diameters ≥ 20 km. For each impact crater that matched our selection criteria, we determined the crater rim azimuth distribution.

For this study, our impact crater selection criteria included the following.

Criterion 1. The crater must overprint, and not be cut by, the lobate scarp. This stratigraphic relationship indicates that the lobate scarp existed before the impact event took place.

Criterion 2. The crater rims must not be cut or offset significantly by faults (unrelated to the lobate scarp). This criterion is based on the fact that postimpact-forming faults that cut across craters alter their plan-view morphologies (Galluzzi et al. 2015) and therefore may affect the results in later steps that involve accessing the rim azimuth distributions of these craters.

Criterion 3. For a similar reason to criterion 2, the crater rims must not be notably cut by overprinting large craters. The presence of these overprinting craters would be associated with large sections of missing rims of the crater in question, making analyses of rim azimuths challenging in later steps.

Criterion 4. The crater must be ~ 20 km or larger in diameter. Because such a large number of craters are present on Mercury's lobate scarps, we are investigating craters of this size, which provide us with a large data set to analyze for purposes of this work. Analyses of smaller craters are beyond the scope of this project and will be assessed in future work.

3.2. Image Selection and Processing

All impact craters that meet our selection criteria were identified by utilizing the MErcury Surface, Space ENvironment, GEochemistry and Ranging (MESSENGER) Mercury Dual Imaging System (MDIS) Global Basemap (~ 116 m pixel $^{-1}$), also called the Morphology Mosaic, published in 2016 and available through the United States Geological Survey Astrogeology branch (Murchie et al. 2016; Hawkins et al. 2007; Denevi et al. 2016) and the Mercury Application of JMARS (Christensen et al. 2009). We then analyzed all individual MDIS images that cover each crater of interest to further investigate the craters that meet the selection criteria. Each crater used in this

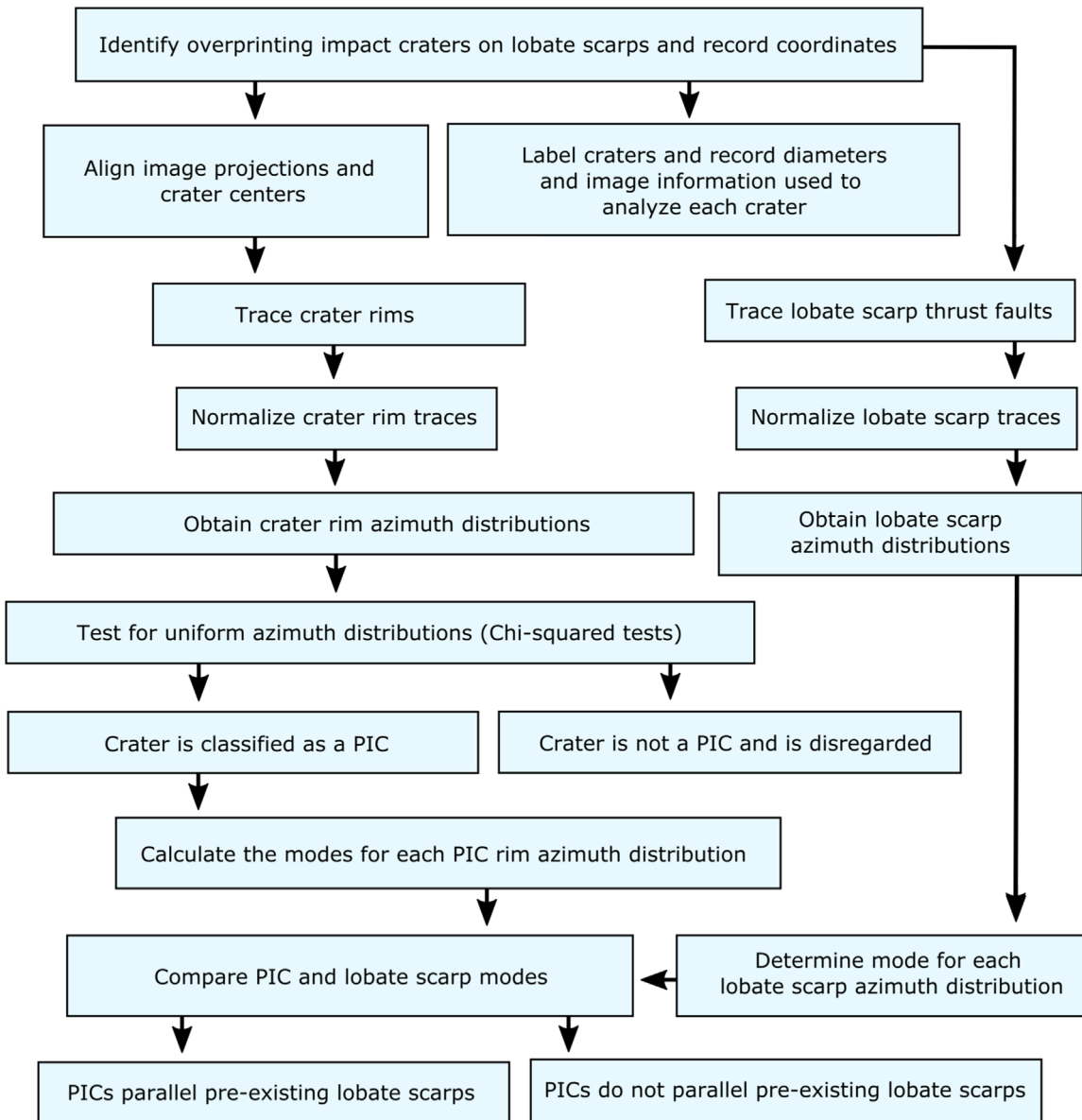


Figure 3. Flowchart illustrating our methodology.

study was subsequently assigned a unique label for organizational purposes in this study (Appendix Table A1).

We utilized the highest-resolution MDIS images available that cover each selected impact crater overprinting a lobate scarp (Appendix Table A1). In some cases, multiple MDIS images were acquired for analyzing individual crater and lobate scarp sets. For example, multiple images were needed if a single image did not cover the entire crater, or if multiple images were needed to investigate the crater and a sufficient length of the adjacent lobate scarp. Additionally, in some cases multiple images were needed if different lighting conditions were more favorable for analyzing the lobate scarp than for the crater. All images used are detailed in the Appendix (Table A1). These MDIS images were downloaded from the Planetary Data System website.⁴ We utilized these images for measurements using the Quantum Geographic Information System software (QGIS Development Team 2021).

Processing and projection of MDIS images were conducted using the Integrated Software for Imagers and Spectrometers 3, version 4.2.0 (Anderson et al. 2004). The images were associated with a camera model for MDIS and augmented with spatial information (geometries of the spacecraft, Sun angle geometries, ground positions, etc.). Because the geometries of surface features are most accurate, with negligible distortion, at the projection center, we projected each overlying MDIS image to the coordinates at the center of each impact crater using a sinusoidal projection. This technique allowed for high-accuracy azimuth measurements to be taken along the crater rims, which was critical for this analysis.

3.3. Crater Rim Tracing

Each impact crater rim was manually traced, as illustrated in Figure 4. We utilized shadowing and lighting variations as high-elevation indicators associated with the crater rims. The resultant crater polygons from this tracing step were then converted to sets of multilines by splitting the continuous

⁴ <https://pds.nasa.gov>

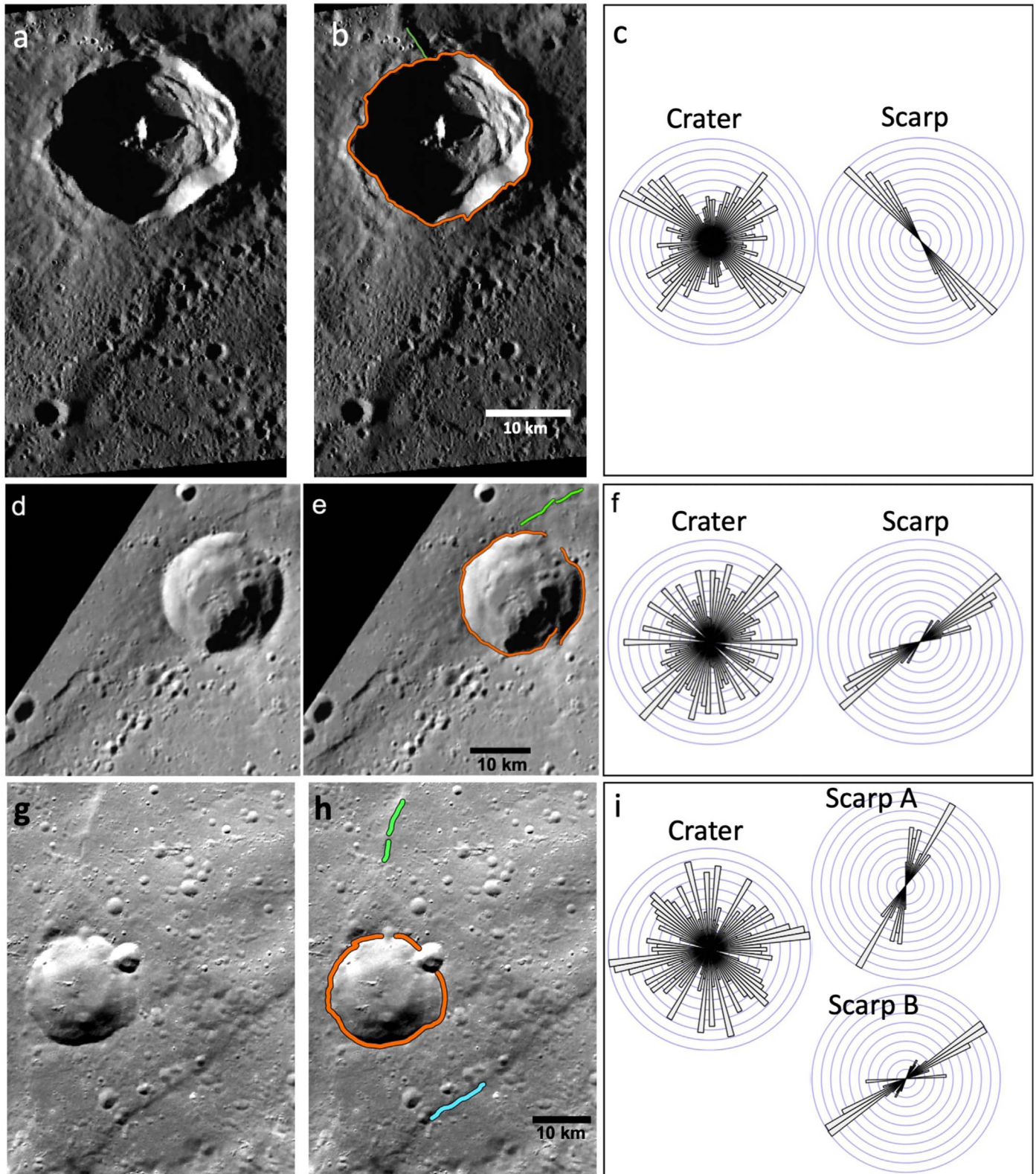


Figure 4. Illustrations of the methodology for analyzing crater rim and nearby lobate scarp azimuths. Only the closest visible sections of each lobate scarp analyzed were investigated to better compare with PIC straight rim segments, as described in Section 3.4. (a) An example of the most common scenario in this study, where an impact crater (crater 3), uncut by extensional faults, other lobate scarps, or craters, overprints a single lobate scarp. (b) The traced crater (orange) and the section of the lobate scarp immediately adjacent to the crater (green) shown in panel (a). (c) Rose diagrams illustrating the azimuth distributions of the crater and lobate scarp traced in panel (b). (d) An uncommon example in this study, showing a crater (crater 1) that has visibly offset rim segments and is overprinting a lobate scarp. (e) The traced crater (orange) and the section of the lobate scarp immediately adjacent to the crater (green) from panel (d). (f) Rose diagrams illustrating the azimuth distributions of the crater and lobate scarp traced in panel (e). (g) An uncommon example in this study, showing a large crater (crater 2) with rim segments that are overprinted by smaller craters. Two nearby lobate scarps are equidistant to the large crater. (h) The traced crater (orange) and the sections of the two lobate scarps that are equidistant to the crater (green and cyan) shown in panel (g). (i) Rose diagrams illustrating the azimuth distributions of the crater and lobate scarps traced in panel (h).

polygon boundaries at their vertices. The numbers of vertices were determined based on the image resolutions (Table A1), where the distance between vertices is equivalent to the distance across a pixel. For each set of multilines, the azimuths of each individual segment were calculated. Each set of multiline segment azimuths and their associated lengths were exported to R for statistical analysis.

The crater rim tracing procedure was not affected by variations in image illumination angles. PICs are easier to recognize by eye in images with low illumination angles where prominent shadows are present along crater rims. However, studies have shown that, when rim azimuths are measured quantitatively, neither image resolution nor solar illumination effects due to lighting geometry have a strong effect on whether or not a crater is identified as a PIC (Binder & McCarthy 1972; Öhman et al. 2006). Measured rim azimuth distributions of impact craters taken on images with low illumination angles have been shown to be statistically similar to those taken on images with high illumination angles (Öhman et al. 2006).

None of the impact craters that we analyzed were notably cut by large extensional faults, lobate scarps, or large craters (see Section 3.1 above). In the majority of cases, the analyzed crater rims also were not cut by smaller features (Figure 4(a)). However, some craters that we analyzed were cut by small features, including faults or mass wasting features (Figure 4(b)) or small craters (Figure 4(c)). In these locations, the small sections of the crater rims erased by these features were excluded from our azimuth distributions (Figures 4(e) and (h)).

3.4. Lobate Scarp Tracing

Similar to our methodology for tracing crater rims, we also traced the structures associated with lobate scarps. We traced the thrust fault surface breaks exposed at the bases of the forelimbs, which are the steeper faces of the lobate scarps. We used shadowing and/or lighting of the surface topography as a guide. However, in some cases, identifying lobate scarp traces was more difficult than tracing impact crater rims due to their more shallow and subdued topography. In some images, shadows and variations in apparent surface brightness, caused by this more subdued topography, were less prominent and therefore more difficult to assess. Because the topography of lobate scarps includes a broad, gently dipping back limb and a steep forelimb, it was critical for us to utilize images with the appropriate lighting geometry.

Lobate scarps are mostly easily recognizable and traceable in images with lighting geometries that allow shadows to be cast along their steep sides, where the fault breaks the surface. Therefore, the direction of sunlight in an image must be from the direction of the shallow back limb in order for us to make use of this shadowing for purposes of tracing lobate scarps. To mitigate this issue, we investigated multiple MDIS images with different lighting geometries covering each lobate scarp (see Section 3.2 above). As mentioned in Section 3.2, multiple MDIS images were analyzed for the area covering each lobate scarp to obtain the images with the most ideal lighting geometry for each feature. In some cases, different images were used to trace the lobate scarp fault than what were used to trace the crater rim. The images determined to be the best for these measurements, and therefore utilized in this study, are listed in the Appendix (Table A1).

To compare lobate scarp azimuths to PIC azimuths in later steps, we investigated the segment of each lobate scarp

immediately adjacent to the overprinting crater (Figure 4). Many lobate scarp segments that are immediately adjacent to the overprinting crater are covered by that crater's ejecta blanket (for example, the area south of the crater in Figure 4(a)). As a result, lobate scarp tracing was done along the segments that were not masked by ejecta and as close as possible to the crater (for example, the area north of the crater in Figure 4(a)). In the majority of cases, a single lobate scarp is associated with an analyzed crater (Figures 4(b), (c), (e), and (f)). However, in some cases, the measurable sections of two lobate scarps are equidistant from the crater (Figure 4(h)). In those cases, we incorporated both lobate scarps into our study, which we termed scarps A and B for each relevant study location (Figure 4(i)).

Like our crater rim tracing methodology, the resultant traced lobate scarp lines were converted to multiline sets, and the azimuths of each segment were calculated. For each lobate scarp, the set of azimuths and their associated lengths were exported to R for statistical analyses.

3.5. Chi-squared Tests

To identify PICs, we tested for uniform azimuth distributions for each analyzed impact crater by applying Pearson's chi-squared tests (e.g., Burt et al. 2009). For these tests, we selected alpha levels of 0.05. Therefore, if a resulting *p*-value of the Pearson's chi-squared test is less than the alpha level of 0.05, then there is 95% confidence that the data are not uniformly distributed. For each impact crater trace, the set of multiline segment azimuths and lengths were utilized to test for a uniform distribution of crater rim azimuths, normalized for the lengths of each measurement, using R's *chisq.test* function.

We binned each crater rim azimuth data into 8° and 16° bins. We then applied four chi-squared tests to each crater, shifting the data within the bins by 4° and 8°, respectively. This shifting method allowed us to detect PIC straight rim segments more accurately in the cases where the orientations of these segments fall close to a bin threshold and therefore may otherwise be split across two bins. This methodology also allowed us to account for straight rim segments of different lengths. If the result of a Pearson's chi-squared test supported the null hypothesis, the azimuth distribution of that particular crater was considered to be uniform. In these scenarios, the crater was identified as a CIC. Alternatively, if the test result was significant, then the azimuth distribution was not considered to be uniform, and the analyzed crater was identified as a PIC.

3.6. Comparing PICs with Lobate Scarps

The prominent PIC rim azimuths (also referred to as "straight rim segments") were determined for all identified PICs. The prominent rim azimuth(s) of each PIC is (are) reflected by the mode(s) of the azimuth distributions. The modes for each PIC were determined using R's *dip.test* function (Maechler & Ringach 2013), which applies the dip test of unimodality described by Hartigan et al. (1985). The modes of each lobate scarp azimuth distribution were also determined using this method.

We then compared the prominent PIC rim azimuth(s) with those of adjacent lobate scarps. We did not expect PIC straight rim segments to precisely reflect the orientations of the measured lobate scarp sections, even if the relationship between PICs and lobate scarps is truly parallel. We had this

Table 1
Results Showing the Modes of PIC and Lobate Scarp Azimuths

Crater ID	PIC Modes		Lobate Scarp Modes		Parallel?	Azimuth Difference	
	1st	2nd	A	B		Degrees	No. of Bins
1	36°–42°		48°–54°		Yes	6°–12°	2
2	78°–84°	174°–180°	24°–30°	54°–60°	Yes	18°–24°	4
3	36°–42°		144°–150°		No		
4	0°–6°		12°–18°	60°–66°	Yes	6°–12°	2
11	162°–168°		168°–174°		Yes	0°–6°	1
13	0°–6°	114°–120°	174°–180°		Yes	0°–6°	1
15	6°–12°	84°–90°	18°–24°		Yes	6°–12°	1
16	132°–138°	42°–48°	6°–12°	162°–168°	Yes	24°–30°	5
17	126°–132°	78°–84°	66°–72°		Yes	6°–12°	1
18	0°–6°		54°–60°		No		
21	66°–72°		0°–6°	48°–54°	Yes	12°–18°	3
22	78°–84°	138°–144°	0°–6°		No		
33	66°–72°		0°–6°		No		
34	60°–66°		30°–36°		Yes	24°–26°	5
38	6°–12°		120°–126°		No		
49	144°–150°		168°–174°	114°–120°	Yes	18°–24°	4
51	30°–36°	126°–132°	144°–150°		Yes	12°–18°	3
76	168°–174°		18°–24°		Yes	24°–30°	5
84	54°–60°	138°–144°	174°–180°	36°–42°	Yes	12°–24°	3
102	114°–120°		120°–126°	42°–48°	Yes	0°–6°	1
115	126°–132°		24°–30°		No		
116	120°–126°		6°–12°	54°–60°	No		
122	66°–72°		36°–42°	156°–162°	Yes	24°–30°	5
134	144°–150°		138°–144°		Yes	0°–6°	1
140	0°–6°		138°–144°	24°–30°	Yes	18°–24°	4
145	138°–144°		132°–138°		Yes	0°–6°	1
148	132°–138°		114°–120°	72°–78°	Yes	12°–18°	3
152	120°–126°		12°–18°		No		
159	78°–84°		36°–42°		No		

Note. All craters that have at least one straight rim segment are shown. Information on all 163 craters analyzed is provided in the [Appendix](#).

expectation because the lobate scarps were traced at some distance from the overprinting PICs (see Section 3.4), and the orientations of the lobate scarps can vary slightly across short distances (see the lobate scarps in Figures 4(a)–(h)). We accounted for this expected azimuth spatial variation by allowing for an acceptable range of differences in PIC and lobate scarp straight segment azimuths. As a threshold, we considered PIC straight rim segments to subparallel lobate scarps if the differences between their prominent azimuths fell into a category within five bins or less (out of 60 bins). Because each bin contains 6° of azimuths, this threshold is equivalent to <30°.

4. Results and Discussion

4.1. PICs on Lobate Scarps

As shown in Table 1, 29 PICs overprinting lobate scarps were identified out of the 163 craters analyzed in this study. Therefore, our results indicate that PICs can form on shortening landforms, in some cases. However, because <20% of the analyzed craters are PICs, we find that CIC formation is the most common outcome of impact events on shortening landforms. Of the identified PICs, 21 have one straight rim segment, while eight exhibit two straight segments.

We find that many PIC straight rim segments exhibit parallel relationships with adjacent lobate scarps. Of the 29 PICs identified in this study, 20 exhibit a parallel relationship with an adjacent lobate scarp. Four examples are shown in Figure 5.

See the information provided in the [Appendix](#) for additional details on other PICs that parallel adjacent lobate scarps (Figures A4–A9). As summarized in Table 1, five of the identified PICs exhibit azimuths between 0° and 6° of an adjacent lobate scarp. Four PICs exhibit azimuths between 6° and 12°, four between 12° and 18°, three between 18° and 24°, and four between 24° and 30°.

4.2. CICs on Lobate Scarps

Most impact events that occur on lobate scarps do not form as PICs and instead were identified as CICs. There are multiple possible explanations for this result. Perhaps the craters that form as CICs did so because of one or more of the following reasons. (1) The impact event occurred too far away from the fault surface break and/or folding-associated fractures. In this case, these structures may not be close enough to influence the orientation of the resulting rim during crater formation. Or, few to no fracture sets are present in the anticline overlying the thrust fault. (2) The craters formed too directly on top of the thrust fault. In this case, the associated thrust and many of the associated steep fractures would be oriented perpendicularly to the crater rim, which is not optimal for influencing rim development. Additionally, large portions of the crater rims may have formed too far from the lobate scarp in this scenario and therefore were not affected by the underlying fault and fractures. (3) The craters are too large relative to the lobate scarp, such that they excavated into the footwall of the thrust. (4) The craters are too small relative to the lobate scarp and

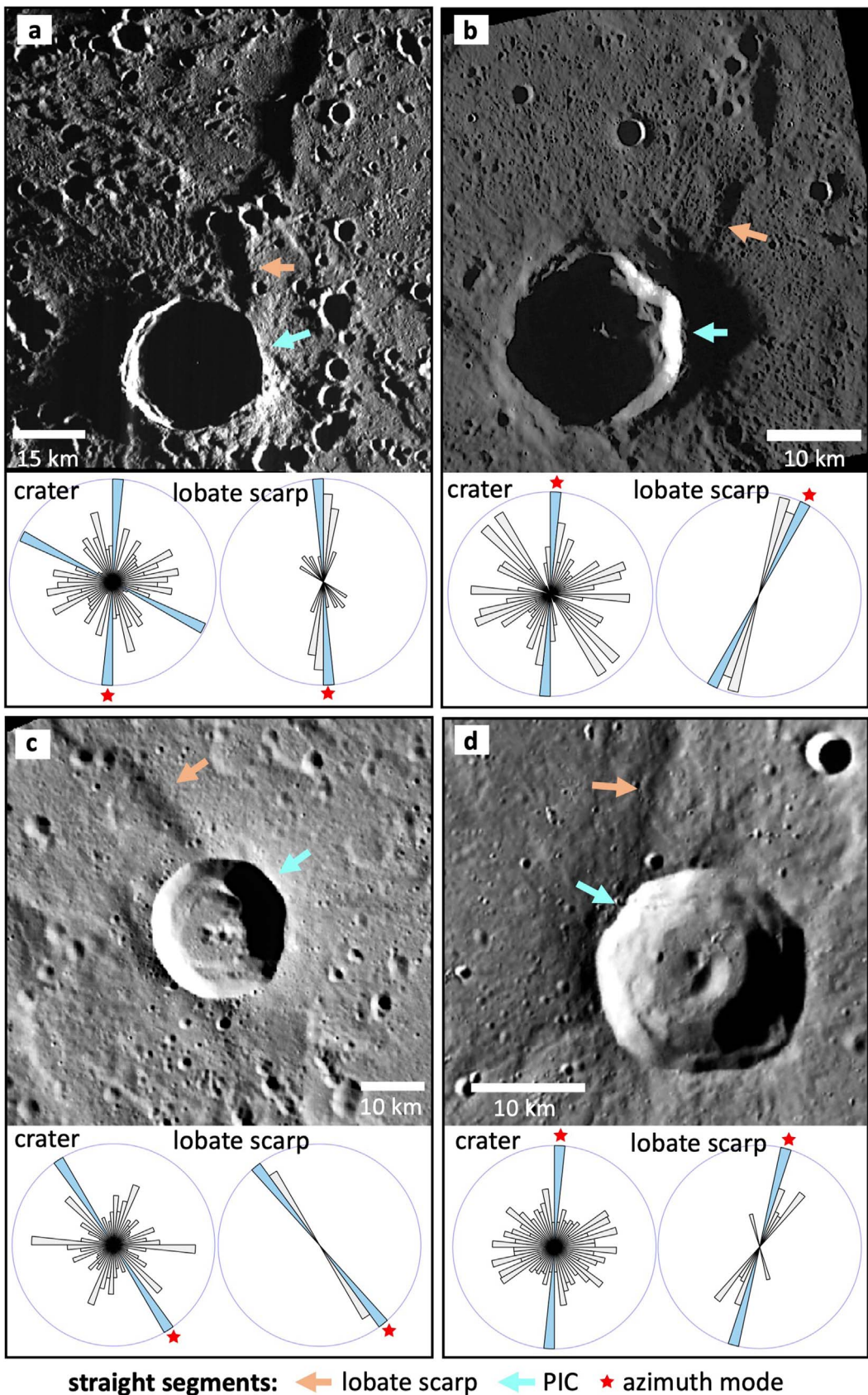


Figure 5. Example illustrations of our results, showing that PICs with straight rim segments parallel adjacent lobate scarps. (a) Crater 13. (b) Crater 140. (c) Crater 134. (d) Crater 4. For a full illustration of our results for all PICs identified, see the annotated rose diagrams in Figures A4–A9. For images of all PICs identified, see Figures A1–A3. See Table A1 for coordinate and image information. See Table 1 for information on azimuth modes, indicating straight segments for all PICs and adjacent lobate scarps analyzed.

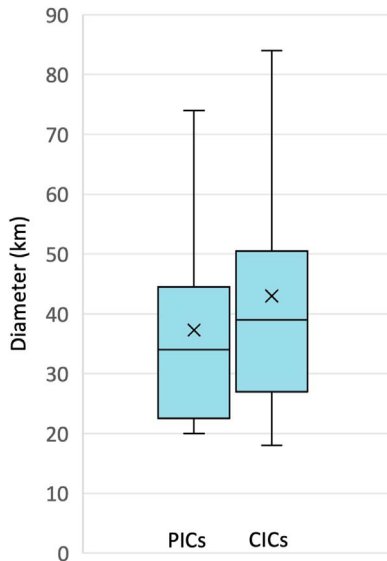


Figure 6. Box-and-whisker plots of PIC and CIC diameters. See Tables A1 and A2 for crater diameters and classifications, respectively. The crosses in the blue boxes represent the means, and the middle horizontal lines represent the modes. The top and bottom lines of the boxes represent the medians of the third and first quartiles, respectively. The ends of the vertical lines represent the maximum and minimum values.

Table 2
Comparison Summary of PIC and CIC Characteristics

	Description	PICs	CICs
Diameter	Minimum	20 km	18 km
	Average	37 km	43 km
	Maximum	81 km	138 km
Lobate scarp–crater intersection	Yes, center	41%	62%
	Yes, edge	41%	10%
	None	31%	43%

Note. Values are provided that show the percentage of PICs associated with lobate scarps that run approximately through the crater center and crater edge and outside the crater edge (none). See Figure 7 for an illustration of these geometries. The percentages along each column, for PICs and CICs, add up to over 100% because some craters are associated with multiple lobate scarps. For additional information on these descriptions, see the caption of Figure 7. Also, see Appendix Table A3 for the data used to derive these results.

therefore did not interact with the underlying thrust fault or fractures. (5) Our methodology is conservative; therefore, some straight rim segments may not have been identified. For example, straight rim segments and PICs may not have been identified if the crater is highly degraded, the straight segment does not take up a large enough portion of the crater rim, or the MDIS image resolution is low relative to the crater size.

We investigated the above possible explanations for CICs on lobate scarps by comparing the study location characteristics of identified PICs with those of CICs (Table 2, Figure 7). We did not find a notable relationship between crater diameter and crater shape (Figure 6). Identified PICs range in diameter from ~ 20 to 81 km, with the average being 37 km. In comparison, diameters of CICs range from ~ 20 to 138 km with an average of 43 km.

We also investigated more specific relationships between craters and adjacent lobate scarps (Figure 7; Tables A3 and

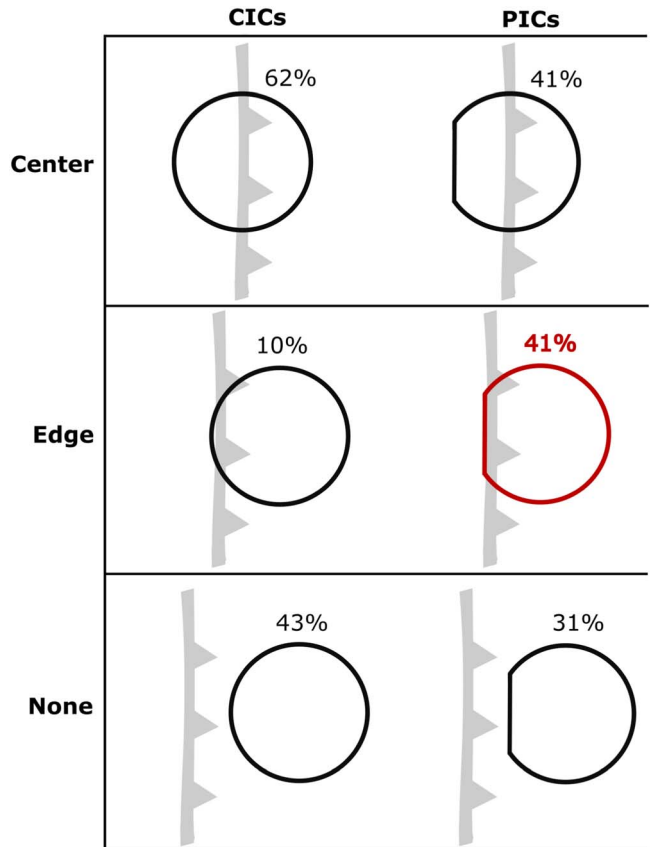


Figure 7. Illustration of crater and surface thrust fault configurations. Also see Table A3. The surface thrust faults associated with the lobate scarps are shown in gray. The values indicate the percentage of particular configurations between the craters and lobate scarp surface thrust faults (center, edge, or none) with the identified crater geometry (PIC vs. CIC). The percentages for PICs and CICs each total more than 100% because some craters were associated with multiple lobate scarps. Our results indicate that, when an impact event occurs on top of a surface thrust fault, the resulting crater will be more likely to form a PIC than a CIC if the center of the impact is offset from the surface thrust fault (see red crater). In this scenario, 41% of PICs identified exhibit this configuration with at least one lobate scarp surface thrust fault. In comparison, only 10% of CICs exhibit this configuration. In Figure 5, three of the four examples shown of PICs overprinting lobate scarps fall into this “edge” category (panels (a), (b), and (d)), while only one example falls into the “center” category (panel (c)).

A4). We categorized lobate scarps with a surface thrust fault that (1) intersects the crater through the crater center, (2) intersects the crater along the crater edge, and (3) does not intersect the crater. In the latter case, while the crater overprints the lobate scarp, the associated surface thrust fault does not directly underlie the crater. Therefore, the crater in question is instead overprinting a subsurface thrust fault in these locations.

We found a small difference in percentage of PICs and CICs that are associated with crater center intersections with lobate scarp surface thrust faults. These cases are associated with 41% of identified PICs and 62% of identified CICs. We also found only a small difference in the percentage of PICs and CICs associated with nearby surface thrust faults but without direct intersections with these faults. These configurations are associated with 31% of PICs and 43% of CICs. We found a notable difference in crater geometries that have edge intersections with surface thrust faults. In these scenarios, 41% of identified PICs are associated with at least one lobate scarp surface thrust fault that skims the crater edge, while only 10% of CICs exhibit this configuration. Therefore, our results

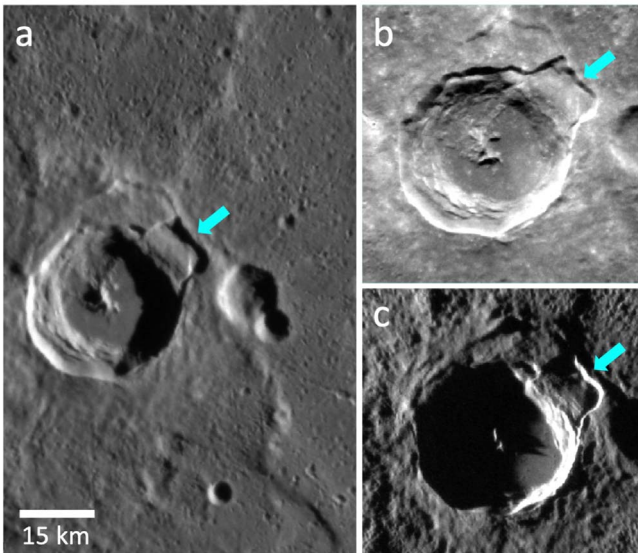


Figure 8. Example of a crater with evidence for wall slumping associated with a straight crater rim segment. Here we show crater 122 ($D = 34$ km) in different MDIS images with differing lighting geometries. Perhaps this crater represents an example of an intermediate step of PIC straight rim segment formation during the crater modification phase, which would support model C for PIC formation (e.g., Schultz 1976; Eppler et al. 1983; see Section 2.2) for PICs associated with thrust faults. MESSENGER MDIS images (a) EN0227933432M, (b) EN0245441590M, and (c) EN0219610891M.

indicate that in the presence of shortening structures, PICs are most likely to form when the impact event occurs so that the resulting crater center is offset from the lobate scarp surface thrust fault.

However, we also find that PICs form in other configurations (center and none in Figure 7). Perhaps PICs on structures accommodating shortening form when an impact event causes the crater walls to interact with the shallow subsurface portion of thrust faults. Alternatively, perhaps these PICs form as a result of interactions with secondary structures instead of the main thrust fault. For example, perhaps the presence of extensional fractures, thought to form in response to lobate scarp formation (Figure 2; e.g., Engelder & Geiser 1980; Klimczak et al. 2019), resulted in some impact events occurring in these contractional terrains to form as PICs. In other words, on shortening landforms, PICs may be most likely to form when the crater edge overprints a surface thrust fault and/or overprints the fractures associated with the thrust's overlying fold.

4.3. Implications for PICs and Lobate Scarps

Our results indicate that impact events commonly produce PICs when the impact center location is slightly offset from the lobate scarp surface thrust fault (see red PIC illustration in Figure 7). This geometry allows the resulting crater rim to interact with the fault.

Some past studies conclude that complex PICs form from normal faulting during the modification stage of crater formation (model C in Section 2.2; e.g., Schultz 1976; Eppler et al. 1983), while other studies instead conclude that they form from thrust faulting during the excavation stage (model D in Section 2.2; Öhman 2009; see Section 2.2). Öhman (2009) makes the argument that the fact that the straight rim segments of PICs are topographic highs indicates that thrusting is necessary, thereby supporting model D.

However, in this work, we note an example of a PIC where crater wall slumping appears to be associated with the formation of an impact crater straight rim segment. In this example, one part of the crater rim appears to have partially formed a straight rim segment but exhibits “failed” slumping (Figure 8). Perhaps this crater represents an example of an intermediate step of PIC straight rim segment formation during the crater modification phase. This slumping may be the result of backsliding against the original thrust motion of the fault plane due to the back limb of the lobate scarp being unsupported after crater formation, similar to slip sheets and collapse folds observed on Earth (Perucca et al. 2016; Harrison & Falcon 1934, 1936). These observations support model C, that modification stage normal faulting forms complex PIC straight rim segments. Based on our observations coupled with the logic described by Öhman (2009), we make the interpretation that both the excavation (model D) and modification (model C) stages of complex PIC crater formation contribute to the formation of the straight rim segments in the presence of thrust faults.

As described in Section 4.3, perhaps the presence of joints associated with folding during lobate scarp formation explains the formation of PICs in other configurations (“center” and “none” categories illustrated in Figure 7). These PICs, which commonly show parallel relationships with adjacent lobate scarps, form as a result of the existence of small joints that trend parallel to the underlying thrust fault or fold hinge. Additionally, perhaps the parallel relationships in these scenarios between PICs and lobate scarps indicate that joints related to anticline formation more often form parallel than obliquely to the fold axes of Mercury’s lobate scarps.

Folding in the brittle parts of the lithosphere is widely known to be accommodated by fractures (e.g., Engelder & Geiser 1980), and many fracture orientations within folds exist (e.g., Klimczak et al. 2019). Therefore, perhaps these particular PICs are highlighting the internal structural architecture of these thrust-fault-related landforms. Perhaps PIC straight rim segments that are aligned with lobate scarp orientations indicate that pure shear accommodates folding and that folding, fracturing, and faulting are coincident within lobate scarps on Mercury.

Perhaps PICs with straight rim segments that are oriented obliquely to adjacent lobate scarps are reflecting fractures unrelated to the lobate scarp. Perhaps they are instead reflecting prefolding and/or postfolding stress directions that generated tectonic fabrics prior to or following lobate scarp formation. Alternatively, these PICs may be reflecting joints associated with anticline formation but with orientations that formed obliquely to the underlying thrust fault. In future studies, the locations and orientations of PICs with straight rim segments that are oblique to the lobate scarp could be evaluated to investigate the orientations of additional stress directions in these locations.

4.4. Comparison with Extensional Settings

Similar to our results for contractional settings, both CICs and PICs form in targets that exhibit extensional fractures and faults. There are many known causes for the formation of CICs in extensional settings, which have been noted on many planetary bodies and in physical laboratory experiments. For example, within the pervasively fractured Wispy Terrain on Dione, 76% of the impact craters analyzed were classified as

PICs, while 24% were classified as CICs. In Dione's more subtly fractured "Non-Wispy Terrain," percentages of PICs are as little as 20% in some locations, where fractures were inferred (Beddingfield et al. 2016). Within Miranda's cratered terrain, which exhibits a large number of fractures of various sizes, only 29% of the identified craters were identified as PICs (Beddingfield & Cartwright 2020). However, the locations of fractures in these terrains relative to each crater analyzed are not as well constrained as those for Dione's Wispy Terrain. Therefore, the true percentage of PICs overprinting extensional features may be higher.

Many characteristics of prefractured target material have been attributed to the formation of CICs. As summarized in Fulmer & Roberts (1963), CICs are shown to form in fractured material if the target consists of a complex set of closely spaced fractures, very widely spaced fractures, or unconsolidated material (Fulmer & Roberts 1963). For example, joints and normal faults both form in response to extensional stresses on planetary bodies. If joints or normal faults are covered by a thick layer of regolith, comparable to or greater than the depth of the impact crater, then we would expect an impact event to form a CIC instead of a PIC.

CICs may also be more likely to form if the impact event creates a crater that is too large or too small relative to the fracture sizes and/or spacing (see Öhman et al. 2005 for a full summary). As summarized in Öhman et al. (2005), in many extensional settings, PICs are somewhat constrained to specific crater diameter ranges. For example, Schultz (1976) concluded that lunar PICs more often exhibit diameters of >1 and <15 km. Similarly, in the Argyre region on Mars, the majority of identified PICs fall within the 10–35 km diameter size range (Öhman et al. 2006).

The explanations for the presence of overprinting CICs along with PICs in extensional target material may provide explanations for the abundant CICs that we identified in contractional settings this work. If similar relationships between CICs and tectonic structures hold true for thrust faulting, then our finding of a large number of CICs relative to PICs is not surprising. In the case of lobate scarps on Mercury, thrust faults are more widely spaced than many of the extensional terrains on planetary bodies noted above. Therefore, we would expect a lower ratio of PICs relative to CICs on lobate scarps relative to extensional terrains. However, additional studies that investigate the relationships between CICs and the characteristics of contractional terrains are needed.

4.5. Applications for Future PIC Interpretations

Our results show that, in addition to extensional structures, contractional structures should be considered as possible explanations for the presence of PICs on bodies across the solar system. Our new knowledge of the parallel relationship between PICs and contractional structures can be applied to better interpret tectonic settings and global stress mechanisms on rocky and icy bodies where PICs are present, as described in Section 4.4.

For example, future analyses of other PICs elsewhere on Mercury could be used to obtain a more complete understanding of the extent and orientations of tectonic features, including the possible existence of contractional structures, that are difficult to discern in available spacecraft images. Detection and characterization of the orientations of subtle tectonic systems could help further discriminate between different

tectonic processes. For example, tidal despinning—the slowing of rotation to lock Mercury in its current 3:2 spin-orbit resonance with the Sun—is proposed to have formed a global fracture pattern (Klimczak et al. 2015). If tidal despinning was overprinted by global contraction—the volumetric reduction of Mercury due to long, sustained planetary cooling (e.g., Solomon 1977)—it would utilize and reactivate favorably oriented fracture sets (Klimczak et al. 2015). Therefore, characterization of additional PICs in future work would provide insight into how other tectonic processes, along with global contraction, played a role in shaping the surface of Mercury. Future analyses may also provide insight into the tectonic setting related to Caloris Basin.

Consideration of contractional features in future PIC work could lead to more refined interpretations of global stress mechanisms on many icy bodies where PICs have been identified (see Section 2.3). For example, global stress events such as orbital recession, despinning, volume contraction, nonsynchronous rotation, and true polar wander may create regions of compression in some locations and tension in others (e.g., Collins et al. 2009). However, only extensional tectonic structures associated with regions of tension have been considered when interpreting PICs. For example, previous analyses of PIC locations and orientations on Dione yielded an inferred fracture pattern across the surface that points to satellite despinning and volume expansion (Beddingfield et al. 2016). Using our results, new analyses of these craters could be used to better interpret PICs in regions that would be in compression during these events (see stress maps provided by Collins et al. 2009 and references within).

5. Conclusions

We conclude that the presence of thrust faults and their associated folds and fractures can result in the formation of PICs for complex craters ~ 20 km in diameter or larger. Additionally, we conclude that PIC straight rim segment azimuths exhibit parallel relationships with the controlling thrust fault azimuths, which are also parallel to their overlying fold hinges. These relationships between craters and shortening structures are like the relationships between craters and normal faults and joints observed in laboratory work and on solid planetary surfaces of rocky and icy bodies.

While PICs do form on thrust faults, we find that in most cases CICs form on thrust faults. In extensional settings, CICs are also known to form when overprinting and/or adjacent to normal faults and joints. However, the specific occurrences of PICs relative to CICs in extensional settings is not well constrained; therefore, we are not able to determine if the ratios of PICs to CICs on thrust faults are like those formed by normal faults. Additionally, only some of the PIC straight rim segments identified in this work may have formed as a result of the presence of the lobate scarp thrust fault itself. In addition to the thrust fault, some PICs may have formed in response to interactions with joints related to the formation of the lobate scarp fold. Future work is needed to further investigate this possibility and therefore determine if some PICs overlying lobate scarps can be utilized to better constrain fractured rock masses associated with lobate scarps. Additional work is also needed to determine if the relationship between PICs and lobate scarps holds true for craters with diameters smaller than 20 km.

Acknowledgments

This work was funded by the NASA Discovery Data Analysis Program, grant No. 80NSSC21K1016.

Appendix

Here we provide information regarding the locations of all craters analyzed in this study and the MESSENGER MDIS

images used to analyze each crater (Table A1). See Section 3.1 for information on and justification of our crater selection criteria. Here we also provide all data and results for this work. Results of chi-squared tests (p -values) are provided (Table A2). See Section 3.5 for the description of how these tests were used to identify PICs. Results describing the proximity of lobate scarps to craters are provided in Table A3, results describing lobate scarp dip directions are provided in Table A4.

Table A1

IDs, Coordinates, Diameters, and Details on MDIS Images Used for Each Impact Crater Analyzed in This Work

Crater ID	Latitude (deg)	Longitude (deg)	Diameter (km)	MDIS Image(s)	Image Resolution(s) (m pixel ⁻¹)
1	59.154	129.329	21	EW0215937434G	193
2	54.562	-2.039	22	EW1017441552G	148
3	56.751	-27.343	22	EW0228154808G	122
4	58.885	27.430	23	EW0252639343G	154
5	66.004	43.240	41	EW0219903748G	143
6	60.155	50.586	26	EW0219776192G	167
7	67.140	61.535	25	EW0219648898G	135
8	52.572	68.749	27	EW0219436182G	202
9	55.197	59.299	31	EW0219606184G	187
10	54.281	51.858	30	EW0234791785G	159
11	64.988	71.198	40	EW1028963152D	169
12	66.575	72.450	20	EW0254914294G	198
13	50.735	93.651	32	EW0261828115G	188
14	55.683	123.627	34	EW0231135611G	175
15	62.359	133.491	20	EW1000244400G	201
16	53.737	157.100	67	EW0243997316G	220
17	58.807	160.410	67	EW0218204261I	170
18	50.933	177.261	41	EW0260704693G	112
19	46.621	92.119	32	EN1046571115M	32
				EW0234240064G	186
20	40.930	83.947	45	EW0249585137G	233
21	48.015	64.845	47	EW0234537072G	189
22	48.852	45.471	26	EW0255202026I	152
23	39.281	31.910	80	EW0235088520G	227
24	48.907	13.126	45	EW0250852619G	175
25	41.708	18.162	40	EW0252870070G	223
26	43.413	9.474	77	EW0265773054G	158
27	45.445	17.003	45	EW0250506911G	158
28	46.953	-30.599	41	EW1005255605I	142
				EW0213025742G	140
29	45.368	-28.877	27	EW0212982293G	143
30	44.667	-27.440	48	EW0225863816G	189
				EW0213025827G	154
31	40.401	-137.956	35	EW0247626443I	182
				EW0242881468G	197
32	50.322	-147.845	24	EW0260215030G	111
				EW0257938432G	299
				EW0257938432G	299
33	47.375	-147.514	24	EW1021876602B	76
				EW1021876602B	161
34	49.778	-178.178	74	EW0250392934G	197
35	43.703	-178.319	43	EW0228024056G	204
36	44.394	-175.703	26	EW0228024056G	127
				EW0228024056G	209
37	29.548	-169.243	27	EW0248000595I	262
				EN0212676209M	111
				EN0212676120M	118
38	36.219	-164.453	38	EW0247943200G	211
39	34.840	-162.731	27	EW0247914368G	214
				EN0212502490M	102
40	27.216	-162.415	24	EW0247885442G	243
				EN0212502235M	122
41	37.292	-122.951	28	EW0257563816G	181

Table A1
(Continued)

Crater ID	Latitude (deg)	Longitude (deg)	Diameter (km)	MDIS Image(s)	Image Resolution(s) (m pixel ⁻¹)
42	31.976	-104.217	25	EN0211676639M	113
43	34.034	-50.169	26	EW0213373594G	178
44	29.847	-46.943	28	EW0213330191G	197
45	29.185	-20.392	45	EW1005111302G EW0228155201G	193 219
46	32.848	-18.850	39	EW0212808634G	192
47	27.800	-8.952	54	EW0212678355G	233
48	37.976	-7.186	35	EW1002232278G	159
49	34.376	-0.374	35	EN0220762110M EW0242841168G	105 257
50	34.661	7.300	30	EW0235555178G	248
51	31.762	-14.678	46	EN0235850479M	119
52	32.833	12.512	30	EW0235342993G	225
53	38.433	78.785	24	EN0239119260M	52
54	33.247	105.763	24	EW0231395066G	119
55	38.300	103.702	25	EW0246562104G	220
56	34.883	104.984	76	EW1046195252G	232
57	34.647	132.725	42	EW0220936688G	89
58	30.027	137.023	59	EW0248778334G EW0220850326G	256 95
				EW0220807126G	96
59	23.402	145.059	28	EN1014993813M	49
60	25.184	78.418	78	EW0254654238G EN0219222948M	252 120
61	19.666	81.181	24	EW1003613015G	259
62	18.932	53.872	26	EN0219647602M	135
63	18.146	9.143	30	EN0220502267M	74
64	24.470	-44.363	30	EW0213330292G EW0243710758G	226 279
65	25.023	-93.617	33	EN1006291928M EN0226710114M	45 98
66	25.944	-91.851	33	EN0211415553M EN0226710146M	140 95
67	18.421	-165.704	24	EN0212501849M	153
68	12.420	-176.020	47	EN0258224295M EN0212849080M	102 190
69	12.080	-173.783	35	EN0212849200M	182
70	9.277	-169.820	45	EN0260821552M	153
71	7.491	-125.628	27	EN0257562934M EN0227048246M	111 148
72	3.715	-110.357	34	EN0226921108M	155
73	7.857	-78.111	25	EN0226455550M EW0213852099G	139 174
74	4.283	5.285	35	EW1045210266H	164
75	10.191	-3.250	34	EN0220761034M	192
76	10.813	15.155	35	EN0220329070M	173
77	7.615	90.460	56	EW0221628397G	183
78	14.328	132.238	76	EW0236193688G	181
79	13.033	140.368	20	EW0220807454G	159
80	10.791	151.151	27	EN1045270925M	152
81	8.723	147.347	38	EN1045473354M EN0244024694M	164 161
82	3.732	142.625	27	EN1045473354M	164
83	4.711	155.900	55	EW0220505167F	198
84	-3.909	99.502	35	EN1046573179M EW0221499071G	213 252
85	2.900	73.276	44	EN0219094286M	218
86	-7.552	5.611	40	EN1004533697M EN0235553800M	156 183
87	-2.610	-6.049	92	EN0220760132M EN0242841854M	127 50
88	-3.996	-55.949	39	EW0243855215G	242

Table A1
(Continued)

Crater ID	Latitude (deg)	Longitude (deg)	Diameter (km)	MDIS Image(s)	Image Resolution(s) (m pixel ⁻¹)
89	1.488	-75.087	79	EW0224044850G	202
90	-2.349	-76.265	31	EN0242044151M	214
91	-0.067	-96.080	61	EN0211414081M	250
				EN0231475794M	250
92	-3.516	-136.802	26	EN0212284006M	101
93	0.413	-177.472	29	EN0212978685M	253
94	-13.765	-163.437	25	EN0258339504M	99
95	-27.948	-156.249	48	EN0247738212M	278
96	-15.409	7.633	68	EN0220499437M	173
97	-23.306	18.361	55	EN0255168898M	160
				EN0250388819M	238
98	-12.126	98.054	27	EN0247139401M	127
99	-22.655	96.162	25	EN0246880606M	139
100	-19.685	92.238	25	EN0234195338M	233
				EN0247139653M	136
101	-19.707	96.858	18	EN0221499527M	107
102	-17.840	95.463	27	EN0247053204M	130
103	-9.766	111.411	66	EN1016176428M	103
104	-10.014	122.000	39	EN1016031842M	173
105	-26.521	117.897	105	EN1016090430M	114
				EN0264071222M	208
				EN0251488753M	54
106	-16.017	151.961	46	EN1014966566M	198
107	-14.224	171.275	43	EN1014822402M	91
108	-10.362	164.440	38	EN0250538312M	65
109	-33.233	69.967	23	EN1013721837M	209
110	-39.445	53.027	53	EN1034260978M	96
111	-41.271	43.527	41	EN1034636136M	78
112	-30.862	43.310	25	EN0235042831M	156
113	-31.120	23.868	65	EN1034433492M	112
				EN0220023562M	256
114	-38.343	25.606	138	EN0235212049M	171
				EN0235296526M	183
115	-33.941	12.693	81	EN0235382112M	160
				EN0250675342M	160
116	-38.030	-71.317	20	EN0239249914M	171
117	-33.997	-70.225	44	EN0238953124M	160
				EN0238953122M	160
118	-37.659	-83.115	54	EN0229280969M	114
119	-35.238	-85.499	33	EN0229280765M	107
				EN0229065549M	137
120	-30.889	-101.189	42	EN0242040912M	199
121	-41.112	-152.785	60	EN0262859538M	155
				EN0227549830M	262
122	-45.166	-167.943	34	EN0245441590M	111
				EN0219610891M	145
123	-44.667	-165.363	28	EN0219610891M	145
124	-49.316	-145.129	97	EN0263232225M	198
125	-49.013	-75.938	50	EN0239250448M	105
126	-49.167	-73.890	27	EN0239250452M	105
127	-57.842	-5.539	45	EN1034691196M	154
128	-51.672	24.568	60	EN1034576600M	135
129	-49.745	25.983	41	EN1034461127M	143
130	-53.187	57.480	39	EN1034173455M	130
131	-44.166	76.886	47	EN0254534297M	175
132	-48.401	74.282	46	EN0252326154M	124
133	-51.627	108.985	74	EN1012943683M	123
134	-56.575	124.190	21	EN0231656048M	127
135	-68.303	-3.973	41	EN1017417089M	163
136	-72.837	-9.929	21	EN1035007027M	178
137	-79.495	56.116	40	EN0238362031M	185
138	58.282	-177.452	91	EW0213155056G	188

Table A1
(Continued)

Crater ID	Latitude (deg)	Longitude (deg)	Diameter (km)	MDIS Image(s)	Image Resolution(s) (m pixel ⁻¹)
139	61.187	-62.447	84	EW1005774359F EW1008396467L	105 312
140	62.591	-22.179	20	EW0228025130G	114
141	61.702	-20.629	22	EW0228025145G	115
142	52.717	-26.258	30	EW0225863950G EW0251313469G	157 149
143	55.429	7.574	67	EW0220330559G	181
144	54.664	9.812	53	EW0220330559G	181
145	61.871	73.143	32	EW0254856578G	226
146	62.570	72.831	34	EW0234537340G	257
147	48.653	179.440	39	EW0260675925I	116
148	45.836	171.540	43	EW0260819956G	163
149	43.798	159.178	79	EW0248490647I EW0220461325G EW0248519506G	175 75 164
150	42.418	154.842	52	EW1045500922G	184
151	40.460	152.959	57	EW0263756769G EW0220590967G EW0220591013G	174 76 82
152	44.096	152.103	28	EW0220590936G EW0235811292G	73 159
153	39.676	165.743	36	EW0235641649G EW0220331770G	182 86
154	36.569	166.708	40	EW0260906588G EW0235429532G	154 219
155	36.904	166.069	47	EW0260906588G EN1014762926M	154 30
156	38.522	159.295	36	EW0220418202G	89
157	30.417	157.200	34	EW0235769087G	233
158	35.901	145.350	40	EW0220720658G EW0235938728G	87 204
159	43.885	143.280	60	EW0248692273I EW0220720543G	178 73
160	38.696	140.665	30	EW0220763820G	81
161	46.102	134.917	36	EW0248836341I	165
162	15.782	93.808	94	EW0221541858G EW0246937109G	152 220
163	24.760	30.293	55	EW1014300124G	224

Note. For additional details on lobate scarp dip directions, see Table A4.

Table A2
Craters that Exhibit Apparent Straight Rim Segments, Chi-squared Test Results, and Identified PICs

Crater ID	Chi-squared Test <i>p</i> -values				PIC
	8° Bins	8° Bins, Shifted 4°	16° Bins	16° Bins, Shifted 8°	
1	0.0854	0.8356	0.04822	0.6288	Yes
2	0.127	0.5909	0.01688	0.346	Yes
3	0.00533	0.07092	1.22×10^{-6}	0.1927	Yes
4	$<2.20 \times 10^{-16}$	$<2.20 \times 10^{-16}$	$<2.20 \times 10^{-16}$	$<2.20 \times 10^{-16}$	Yes
10	0.658	0.5139	0.1313	0.6288	No
11	0.403	0.4893	0.02437	0.7751	Yes
12	0.810	0.9195	0.4241	0.9108	No
13	0.0756	0.04339	0.01854	0.1052	Yes
15	0.953	0.7826	0.01854	0.9943	Yes
16	0.0155	0.04188	1.16×10^{-5}	0.1423	Yes
17	2.5×10^{-3}	0.03692	0.001196	0.2647	Yes
18	0.0618	0.01433	0.03529	0.5723	Yes
21	0.0339	0.2917	0.07228	0.04627	Yes
22	0.0112	0.01552	1.237×10^{-3}	0.1714	Yes
25	0.404	0.6677	0.2511	0.7243	No
27	0.203	0.9093	0.09669	0.7343	No
33	0.117	0.3967	9.473×10^{-3}	0.4472	Yes
34	0.0148	0.3517	0.1165	0.4938	Yes
36	0.557	0.1966	0.5304	0.308	No
37	0.583	0.6453	0.5461	0.2336	No
38	0.0254	0.2864	6.059×10^{-3}	0.4969	Yes
39	0.119	0.6247	0.1053	0.3678	No
40	0.121	0.9015	0.1016	0.3733	No
44	0.956	0.5043	0.3343	0.9395	No
48	0.336	0.1992	0.095	0.2522	No
49	0.237	0.3685	0.01791	0.5782	Yes
50	0.622	0.7619	0.5373	0.8716	No
51	0.0247	0.04658	6.448×10^{-3}	0.03071	Yes
52	0.361	0.2996	0.2449	0.2994	No
55	0.282	0.282	0.3855	0.4756	No
59	0.183	0.3643	0.2933	0.6253	No
61	0.457	0.5325	0.4708	0.4171	No
64	0.442	0.4947	0.1149	0.7435	No
67	0.458	0.1125	0.4196	0.5119	No
68	0.264	0.7898	0.5093	0.3422	No
69	0.887	0.6514	0.4938	0.8707	No
70	0.209	0.6092	0.06719	0.4907	No
74	0.562	0.6697	0.1232	0.9439	No
76	0.176	0.4208	0.01978	0.2011	Yes
80	0.574	0.574	0.6713	0.8193	No
81	0.542	0.3546	0.4089	0.4907	No
82	0.3905	0.744	0.08995	0.9473	No
84	0.111	0.7795	0.04238	0.4803	Yes
86	0.806	0.7428	0.2268	0.9272	No
94	0.610	0.610	0.4854	0.3857	No
95	0.284	0.7462	0.09876	0.1855	No
98	0.569	0.4144	0.3636	0.9311	No
99	0.349	0.9544	0.1973	0.5132	No
100	0.521	0.8622	0.7365	0.5321	No
101	0.858	0.5414	0.8277	0.9123	No
102	0.0652	0.02155	0.04015	0.03779	Yes
108	0.525	0.6522	0.2082	0.3593	No
109	0.871	0.5886	0.4659	0.9149	No
115	0.0408	0.2987	0.06109	0.2398	Yes
116	4.96×10^{-4}	0.02139	0.0001787	7.27×10^{-3}	Yes
122	0.281	0.3472	0.02725	0.09631	Yes
127	0.305	0.8513	0.3273	0.9563	No
134	0.525	0.6987	0.04132	0.9377	Yes
135	0.438	0.6442	0.5485	0.6288	No
140	2.87×10^{-3}	0.1011	0.004802	0.06413	Yes
141	0.119	0.6983	0.09781	0.7406	No
145	2.31×10^{-3}	0.4041	0.0549	0.4275	Yes
148	0.129	0.8124	9.378×10^{-3}	0.8524	Yes
152	0.161	0.07438	5.24×10^{-3}	0.3582	Yes
153	0.938	0.9644	0.33	0.9755	No
156	0.474	0.588	0.1503	0.8912	No
157	0.854	0.5238	0.9312	0.8438	No
158	0.540	0.2644	0.2016	0.9275	No
159	0.0384	0.3163	1.698×10^{-4}	0.274	Yes

Table A3
Descriptions of Analyzed Lobate Scarp Proximities to Craters

Crater ID	Distance from Measured Lobate Scarp Section to Crater Rim (km)		Intersection between Crater and Lobate Scarp Fault?		Crater Diameter (km)
	Scarp A	Scarp B	Scarp A	Scarp B	
			PICs		
1	1	...	Yes, edge	...	21
2	15	15	Yes, edge	No	22
3	0	...	Yes, center	...	22
4	4	1	Yes, edge	Yes, center	23
11	4	...	Yes, edge	...	40
13	9	...	Yes, edge	...	32
15	11	...	No	...	20
16	41	67	Yes, edge	No	67
17	35	...	Yes, edge	...	67
18	14	...	Yes, center	...	41
21	54	46	No	No	47
22	33	...	No	...	26
33	25	...	Yes, center	...	24
34	12	...	Yes, edge	...	74
38	38	...	No	...	38
49	11	12	Yes, center	Yes, center	35
51	5	...	Yes, center	...	46
76	18	...	Yes, center	...	35
84	8	...	Yes, edge	...	35
102	13	3	No	No	27
115	56	...	Yes, edge	...	81
116	2	13	Yes, center	No	20
122	9	17	Yes, edge	Yes, edge	34
134	3	...	Yes, center	...	21
140	3	9	Yes, edge	Yes, edge	20
145	8	...	Yes, center	...	32
148	12	39	Yes, center	Yes, center	43
152	18	...	Yes, center	...	28
159	21	...	No	...	60
CICs					
5	24	16	No	Yes, center	41
6	18	10	Yes, center	Yes, center	26
7	7	...	No	...	25
8	35	...	Yes, center	...	27
9	13	...	No	...	31
10	16	...	Yes, center	...	30
12	3	...	No	...	20
14	15	...	Yes, center	...	34
19	4	...	Yes, center	...	32
20	76	...	Yes, center	...	45
23	20	...	Yes, center	...	80
24	40	...	Yes, center	...	45
25	60	...	Yes, center	...	40
26	36	...	Yes, center	...	77
27	26	...	No	...	45
28	13	...	Yes, center	...	41
29	8	...	Yes, edge	...	27
30	41	...	No	...	48
31	26	...	No	...	35
32	9	...	Yes, edge	...	24
35	12	...	Yes, center	...	43
36	0	...	Yes, center	...	26
37	19	...	No	...	27
39	11	...	No	...	27
40	12	...	No	...	24
41	19	...	No	...	28
42	9	...	Yes, center	...	25
43	17	...	Yes, center	...	26
44	10	...	Yes, edge	...	28
45	17	...	No	...	45
46	8	...	Yes, center	...	39
47	17	...	No	...	54
48	1	...	Yes, center	...	35
50	16	...	Yes, center	...	30
52	3	...	No	...	30

Table A3
(Continued)

Crater ID	Distance from Measured Lobate Scarp Section to Crater Rim (km)		Intersection between Crater and Lobate Scarp Fault?		Crater Diameter (km)
	Scarp A	Scarp B	Scarp A PICs	Scarp B	
53	14	4	Yes, edge	Yes, edge	24
54	2	...	Yes, edge	...	24
55	10	...	Yes, center	...	25
56	25	...	Yes, center	...	76
57	14	23	Yes, center	No	42
58	30	11	Yes, center	Yes, center	59
59	3	...	Yes, center	...	28
60	19	...	No	...	78
61	8	17	Yes, center	No	24
62	3	...	No	...	26
63	16	...	Yes, center	...	30
64	17	...	Yes, center	...	30
65	30	...	No	...	33
66	20	...	Yes, center	...	33
67	18	10	Yes, center	No	24
68	40	37	No	No	47
69	5	13	Yes, edge	Yes, center	35
70	8	10	Yes, edge	Yes, center	45
71	11	...	Yes, center	...	27
72	13	...	Yes, center	...	34
73	15	1	Yes, edge	Yes, center	25
74	18	...	Yes, center	...	35
75	8	1	Yes, center	Yes, center	34
77	22	...	Yes, center	...	56
78	11	...	Yes, center	...	76
79	3	4	No	No	20
80	13	15	No	Yes, center	27
81	8	...	Yes, edge	...	38
82	6	22	Yes, center	No	27
83	30	...	Yes, center	...	55
85	5	...	Yes, center	...	44
86	35	...	No	...	40
87	73	...	Yes, center	...	92
88	4	...	Yes, center	...	39
89	16	...	Yes, center	...	79
90	8	...	Yes, edge	...	31
91	14	...	Yes, center	...	61
92	14	38	Yes, center	No	26
93	18	23	No	No	29
94	10	15	No	Yes, center	25
95	32	...	No	...	48
96	37	...	No	...	68
97	52	...	Yes, center	...	55
98	14	2	No	Yes, center	27
99	13	...	Yes, center	...	25
100	21	...	Yes, center	...	25
101	9	6	No	No	18
103	12	8	Yes, center	Yes, center	66
104	1	...	Yes, edge	...	39
105	8	...	Yes, center	...	105
106	22	9	No	No	46
107	8	10	Yes, center	Yes, edge	43
108	7	...	Yes, center	...	38
109	5	...	No	...	23
110	13	33	No	No	53
111	26	...	Yes, center	...	41
112	5	8	Yes, center	Yes, center	25
113	3	...	Yes, center	...	65
114	32	...	Yes, center	...	138
117	36	...	No	...	44
118	19	7	No	Yes, center	54
119	26	...	Yes, center	...	33
120	10	...	Yes, center	...	42
121	16	42	Yes, center	No	60
123	13	...	Yes, center	...	28
124	54	...	Yes, center	...	97
125	6	...	Yes, center	...	50
126	17	...	Yes, center	...	27

Table A3
(Continued)

Crater ID	Distance from Measured Lobate Scarp Section to Crater Rim (km)		Intersection between Crater and Lobate Scarp Fault?		Crater Diameter (km)
	Scarp A	Scarp B	Scarp A	Scarp B	
			PICs		
127	4	...	No	...	45
128	16	6	Yes, center	Yes, center	60
129	39	...	No	...	41
130	16	...	Yes, center	...	39
131	20	25	Yes, center	Yes, center	47
132	0	...	Yes, center	...	46
133	5	...	Yes, center	...	74
135	7	...	No	...	41
136	15	...	No	...	21
137	7	...	No	...	40
138	54	...	No	...	91
139	8	56	Yes, center	Yes, center	84
141	1	7	Yes, center	Yes, center	22
142	29	...	No	...	30
143	64	...	No	...	67
144	20	...	Yes, center	...	53
146	24	18	No	Yes, edge	34
147	4	...	Yes, center	...	39
149	37	42	No	No	79
150	15	38	Yes, center	Yes, center	52
151	28	42	Yes, center	Yes, center	57
153	11	13	Yes, center	Yes, center	36
154	90	...	Yes, center	...	40
155	8	...	No	...	47
156	13	...	No	...	36
157	23	32	No	No	34
158	13	20	Yes, center	Yes, edge	40
160	14	...	No	...	30
161	14	...	Yes, center	...	36
162	97	...	No	...	94
163	17	...	No	...	55

Table A4
Dip Directions of Each Lobate Scarp Analyzed

Crater ID	Lobate Scarp Dip Direction	
	Scarp A	Scarp B
1	SE	...
2	NW	SE
3	SW	...
4	E	SE
5	NW	NW
6	W	SW
7	S	...
8	SE	...
9	NW	...
10	NE	...
11	W	...
12	NE	...
13	E	...
14	SE	...
15	SE	...
16	E	E
17	NW	...
18	SE	...
19	NW	...
20	NW	...
21	E	SE
22	SW	...
23	SE	...
24	E	...
25	SW	...
26	E	...
27	NW	...
28	W	...
29	NW	...
30	NW	...
31	SE	...
32	SW	...
33	E	...
34	SE	...
35	SE	...
36	SE	...
37	SW	...
38	SW	...
39	NE	...
40	NW	...
41	W	...
42	E	...
43	SE	...
44	W	...
45	W	...
46	SE	...
47	NE	...
48	SE	...
49	W	SW
50	W	...
51	NE	...
52	E	...
53	NW	E
54	SE	...
55	E	...
56	SW	...
57	E	E
58	W	NW
59	NW	...
60	SE	...
61	E	NW
62	SE	...
63	SE	...

Table A4
(Continued)

Crater ID	Lobate Scarp Dip Direction	
	Scarp A	Scarp B
64	SW	...
65	NW	...
66	SE	...
67	NE	NW
68	NW	SW
69	NW	E
70	NE	NE
71	SE	...
72	NW	...
73	SE	SW
74	E	...
75	NW	NW
76	SE	...
77	W	...
78	SE	...
79	SW	W
80	W	SW
81	NW	...
82	E	SE
83	NW	...
84	E	SE
85	E	...
86	NE	...
87	SW	...
88	SW	...
89	E	...
90	E	...
91	NW	...
92	NE	NW
93	NE	SE
94	E	NE
95	SE	...
96	NE	...
97	NE	...
98	NE	NE
99	SE	...
100	SE	...
101	SE	E
102	NE	SE
103	E	NE
104	W	...
105	W	...
106	W	SW
107	E	NE
108	E	...
109	NW	...
110	NW	NW
111	NW	...
112	E	NE
113	SE	...
114	NW	...
115	NW	...
116	W	SE
117	NE	...
118	NW	NE
119	NW	...
120	NE	...
121	NE	NW
122	NW	SW
123	W	...
124	NE	...
125	NE	...
126	NW	...

Table A4
(Continued)

Crater ID	Lobate Scarp Dip Direction	
	Scarp A	Scarp B
127	SW	...
128	SE	N
129	NW	...
130	SE	...
131	NW	NE
132	SE	...
133	NE	...
134	NE	...
135	SW	...
136	NE	...
137	E	...
138	W	...
139	SW	NE
140	SW	NW
141	SW	NW
142	W	...
143	NE	...
144	NW	...
145	SW	...
146	NE	SE
147	SE	...
148	SE	SE
149	NW	SW
150	SW	NW
151	NE	NW
152	SE	...
153	E	NE
154	NE	...
155	NE	...

Table A4
(Continued)

Crater ID	Lobate Scarp Dip Direction	
	Scarp A	Scarp B
156	W	...
157	W	NW
158	NE	SE
159	SE	...
160	SE	...
161	NE	...
162	NW	...
163	NE	...

Note. See Table A1 for locations of each crater and adjacent lobate scarp.

Annotated portions of MDIS images covering each PIC identified are shown in Figure A1 for craters 1–22, Figure A2 for craters 33–134, and Figure A3 for craters 140–159. Lobate scarps are visible in some of these images; however, in many cases, the scarps are most visible some distance from each crater due to overprinting of the scarps by impact ejecta. See Figure 5 for context images (with lower resolutions) that show PICs with their adjacent lobate scarps in single MDIS images.

Annotated rose diagrams for all PICs analyzed and their associated lobate scarps are provided in Figure A4 for craters 1–11, Figure A5 for craters 13–18, Figure A6 for craters 21–38, Figure A7 for craters 49–102, Figure A8 for craters 111–140, and Figure A9 for craters 145–159. See Table 1 for a summary of PIC straight rim segment azimuths and azimuths of adjacent lobate scarps.

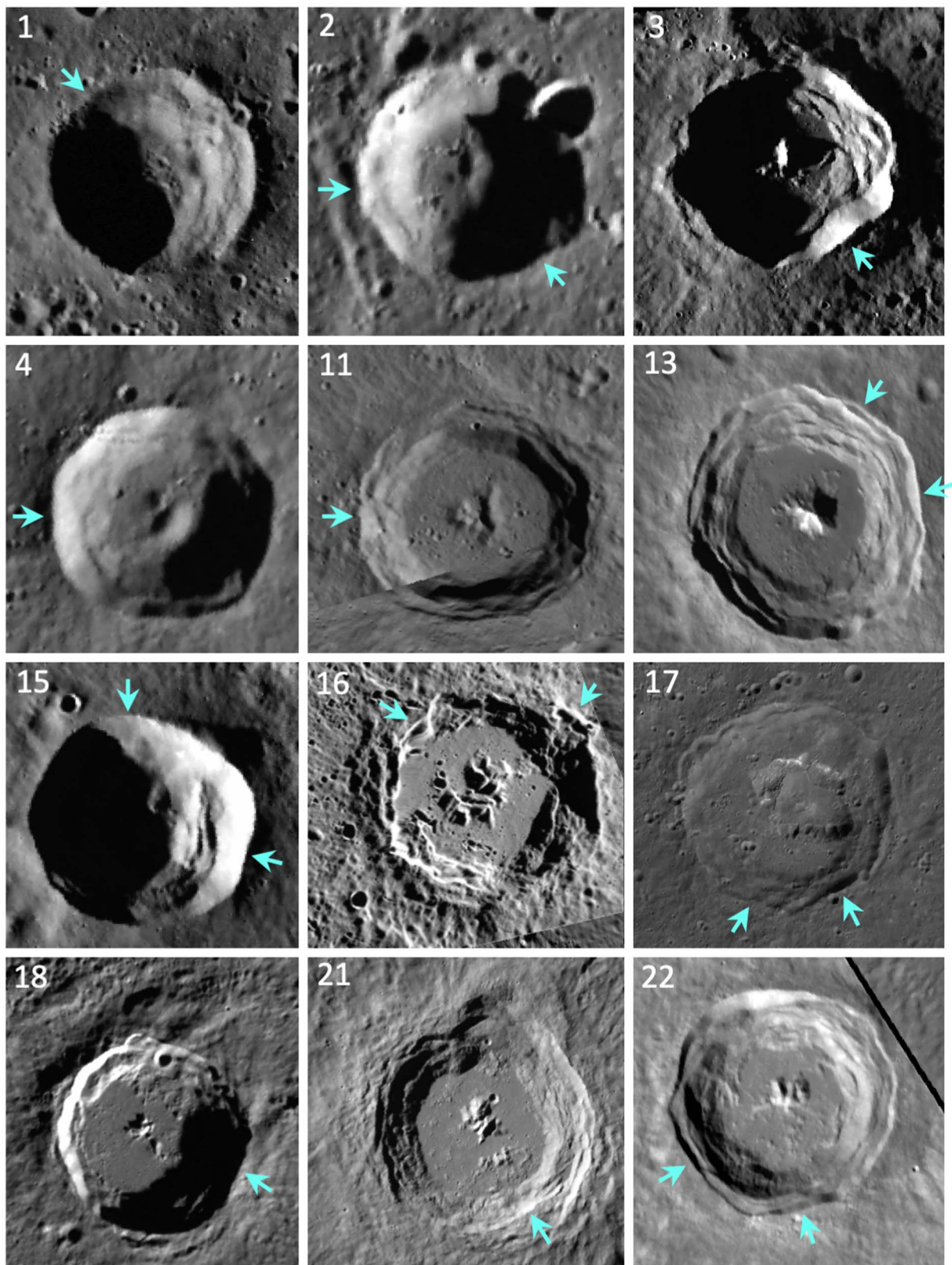


Figure A1. Identified PICs for craters 1–22 (see Table A2). Cyan arrows indicate examples of straight rim segments. See Table A1 for information on PIC locations, diameters, and MDIS image coverage. See Figures A2 and A3 for additional identified PICs.

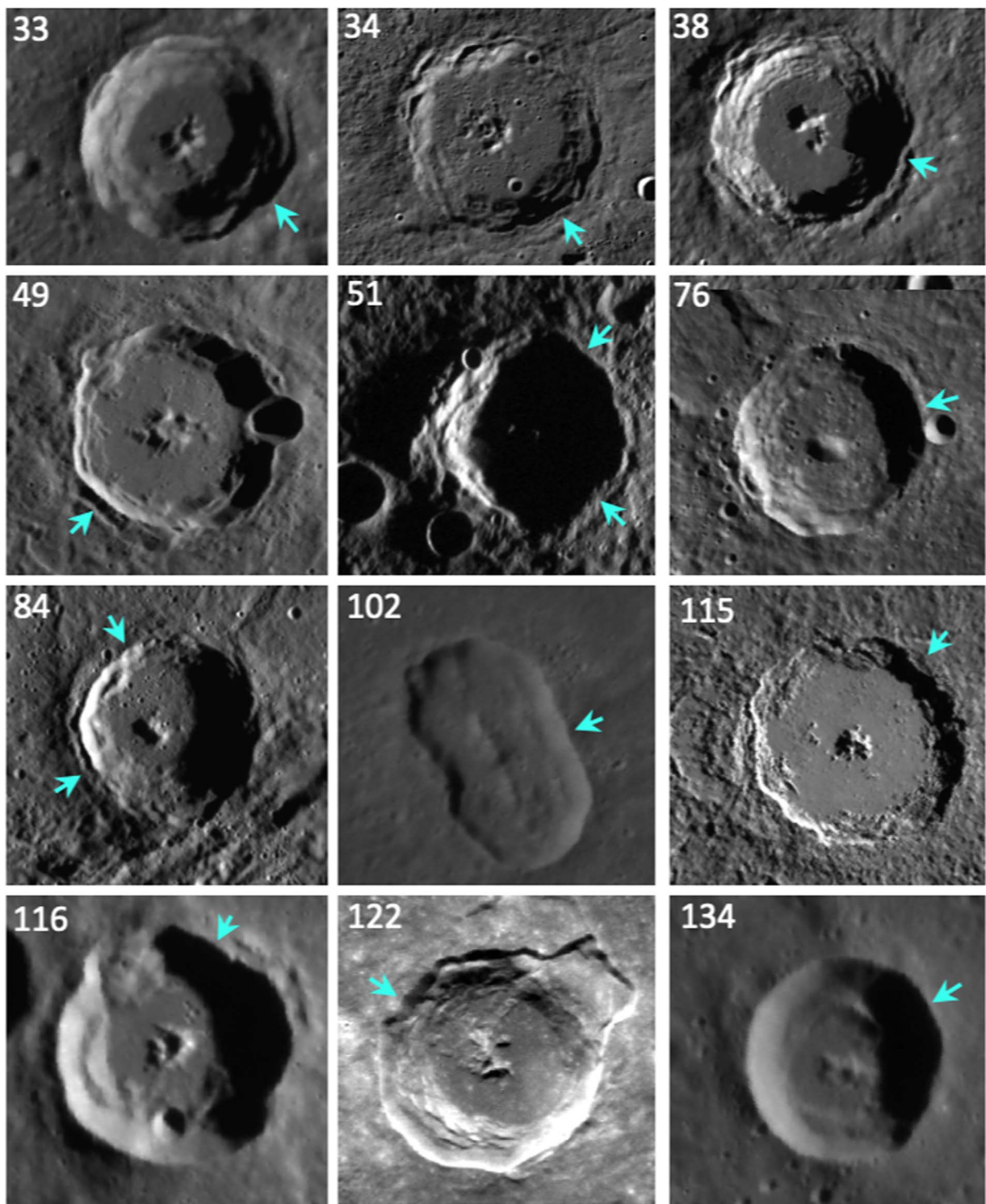


Figure A2. Identified PICs for craters 33–134 (see Table A2). Cyan arrows indicate examples of straight rim segments. See Table A1 for information on PIC locations, diameters, and MDIS image coverage. See Figures A1 and A3 for additional identified PICs.

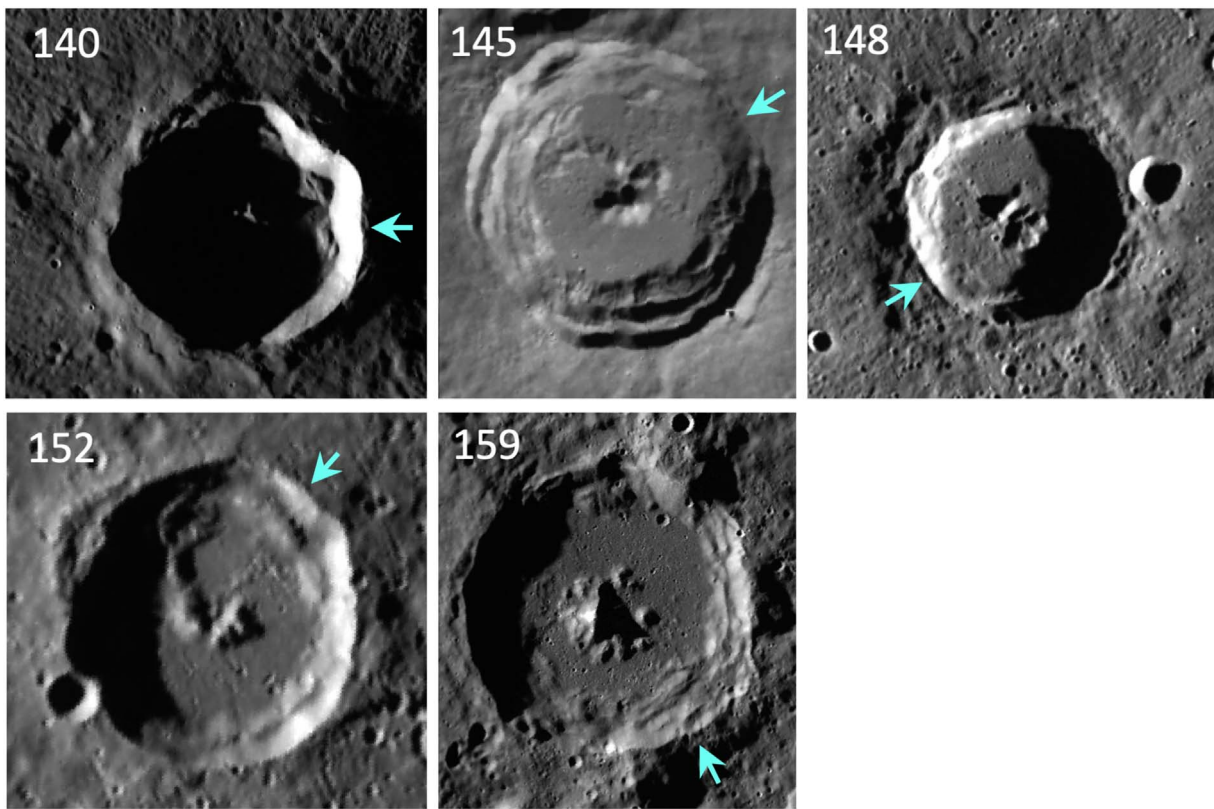


Figure A3. Identified PICs for craters 140–152 (see Table A2). Cyan arrows indicate examples of straight rim segments. See Table A1 for information on PIC locations, diameters, and MDIS image coverage. See Figures A1 and A2 for additional identified PICs.

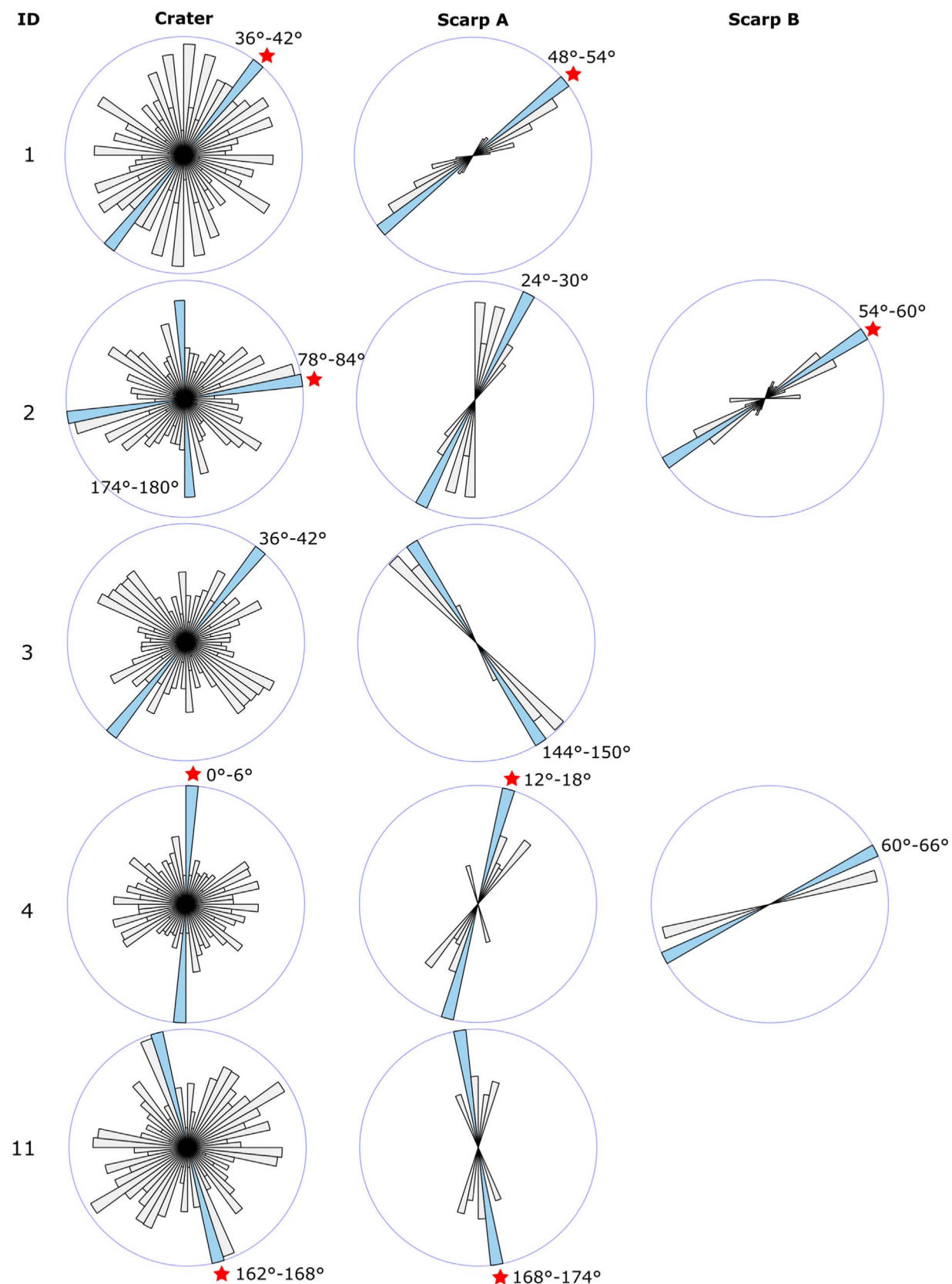


Figure A4. Rose diagrams showing the azimuth distributions of PIC rims and adjacent lobate scarps for craters 1–11 (Table A1). Modes are represented by blue petals, and red stars denote similar orientations between PIC straight rim segments and lobate scarps.

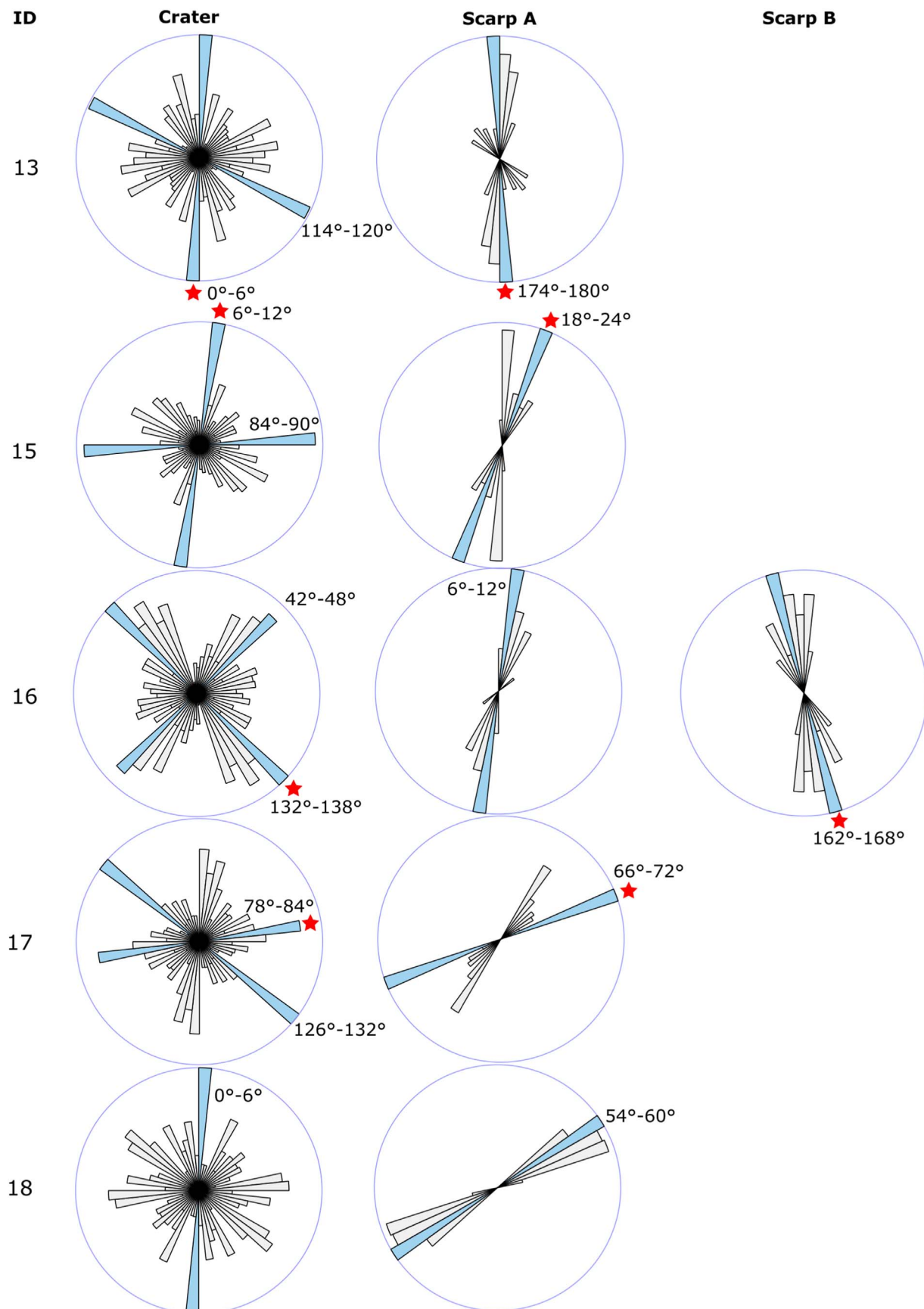


Figure A5. Rose diagrams showing the azimuth distributions of PIC rims and adjacent lobate scarps for craters 13–18 (Table A1). Modes are represented by blue petals, and red stars denote similar orientations between PIC straight rim segments and lobate scarps.

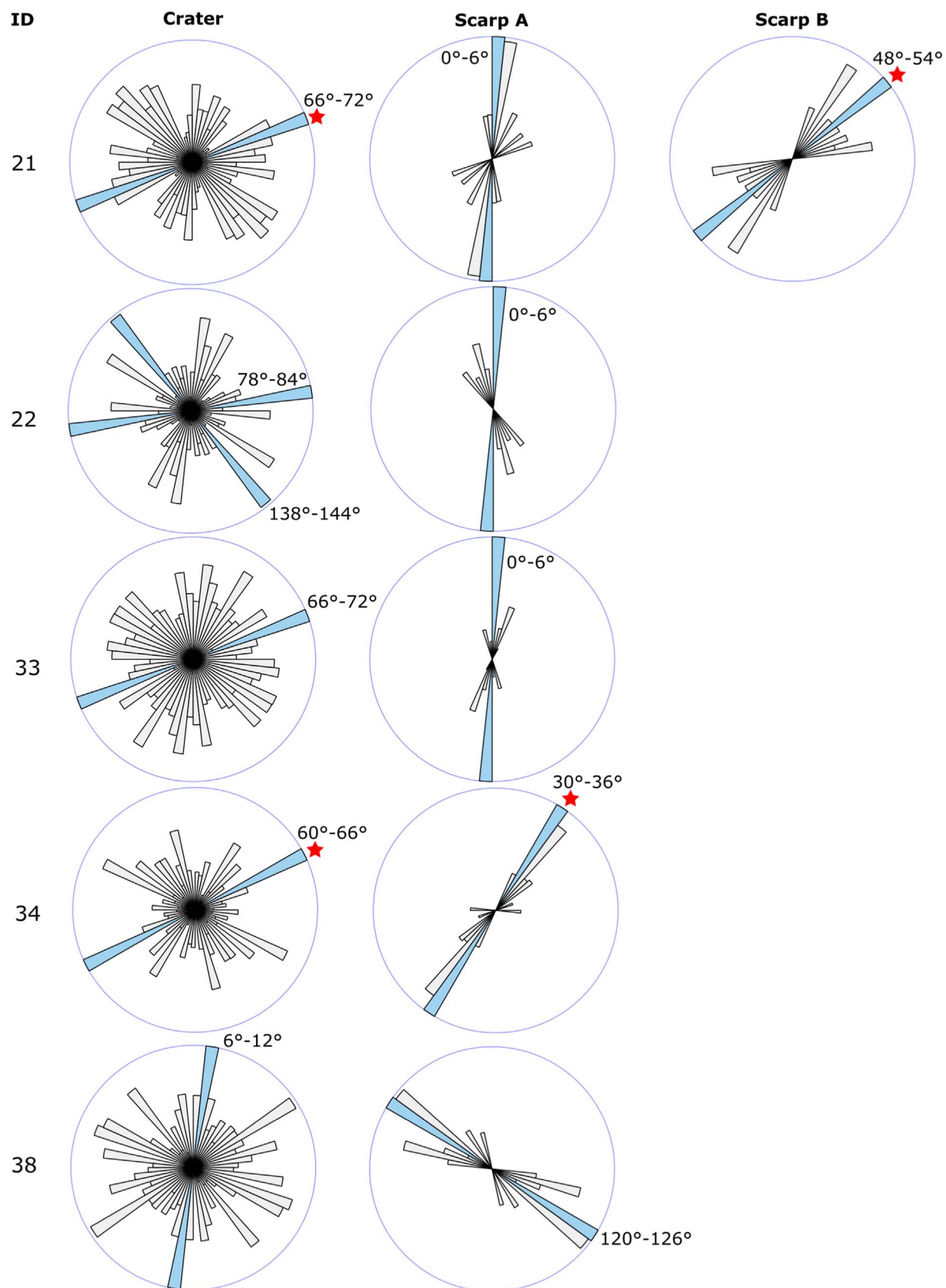


Figure A6. Rose diagrams showing the azimuth distributions of PIC rims and adjacent lobate scarps for craters 21–38 (Table A1). Modes are represented by blue petals, and red stars denote similar orientations between PIC straight rim segments and lobate scarps.

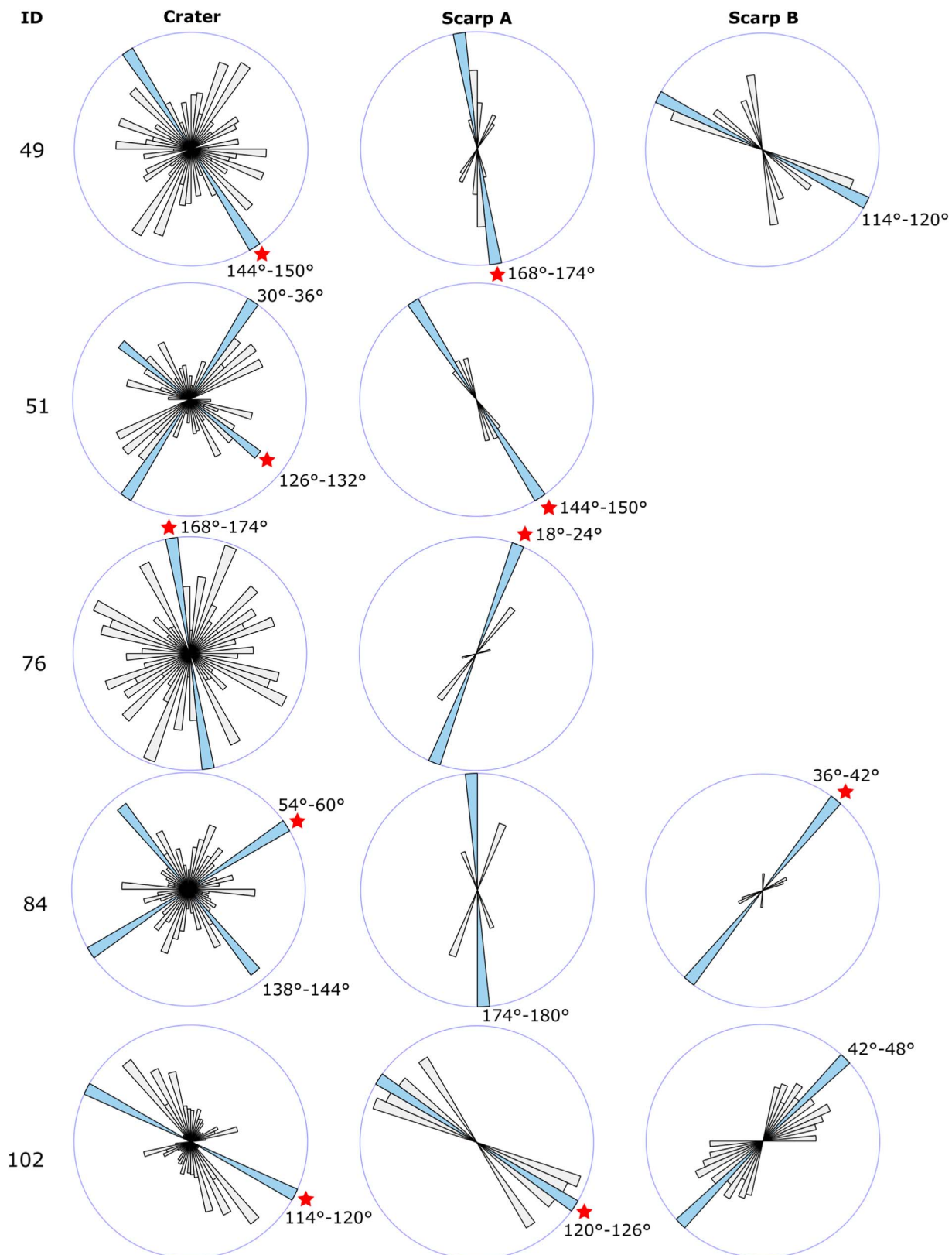


Figure A7. Rose diagrams showing the azimuth distributions of PIC rims and adjacent lobate scarps for craters 49–102 (Table A1). Modes are represented by blue petals, and red stars denote similar orientations between PIC straight rim segments and lobate scarps.

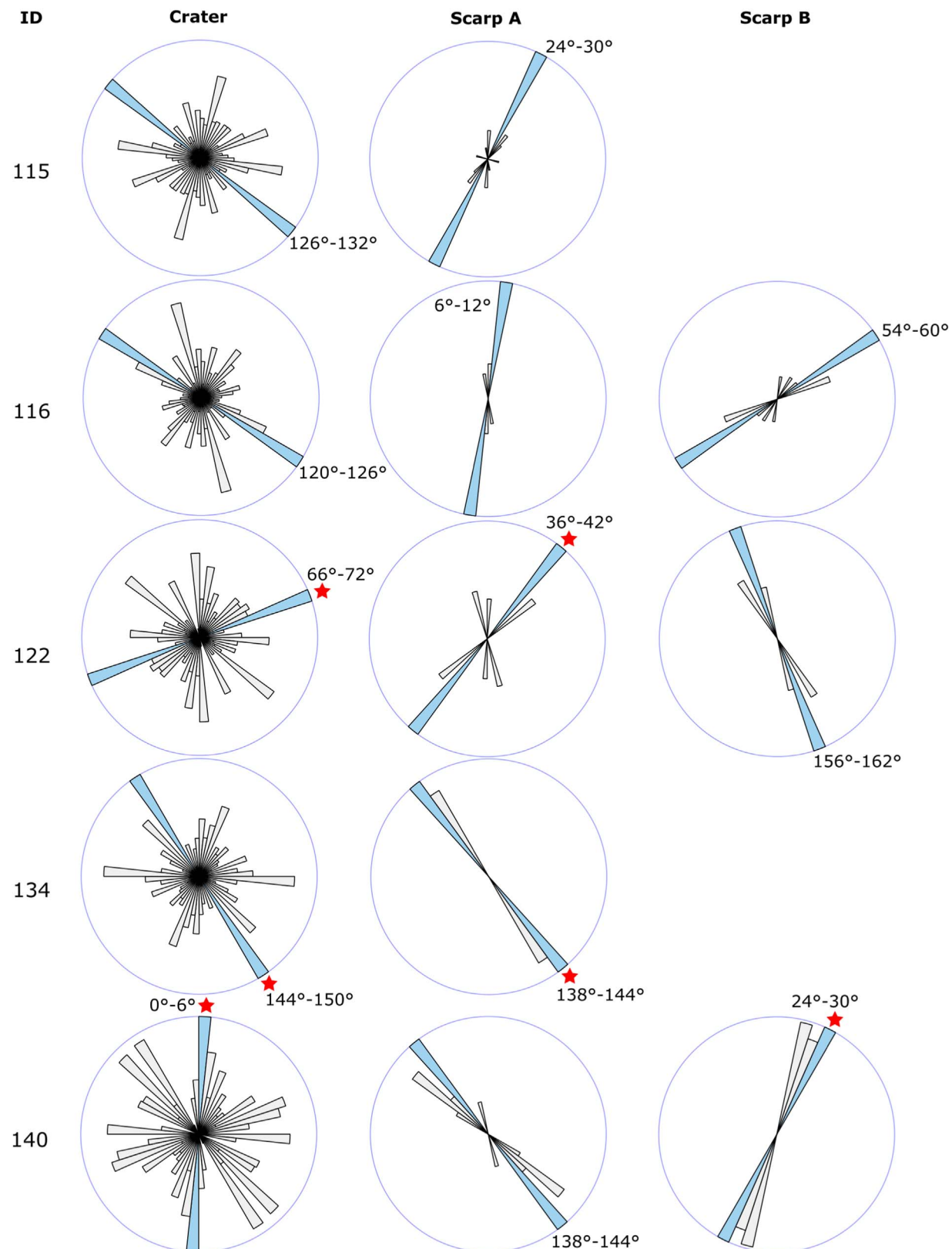


Figure A8. Rose diagrams showing the azimuth distributions of PIC rims and adjacent lobate scarps for craters 115-140 (Table A1). Modes are represented by blue petals, and red stars denote similar orientations between PIC straight rim segments and lobate scarps.

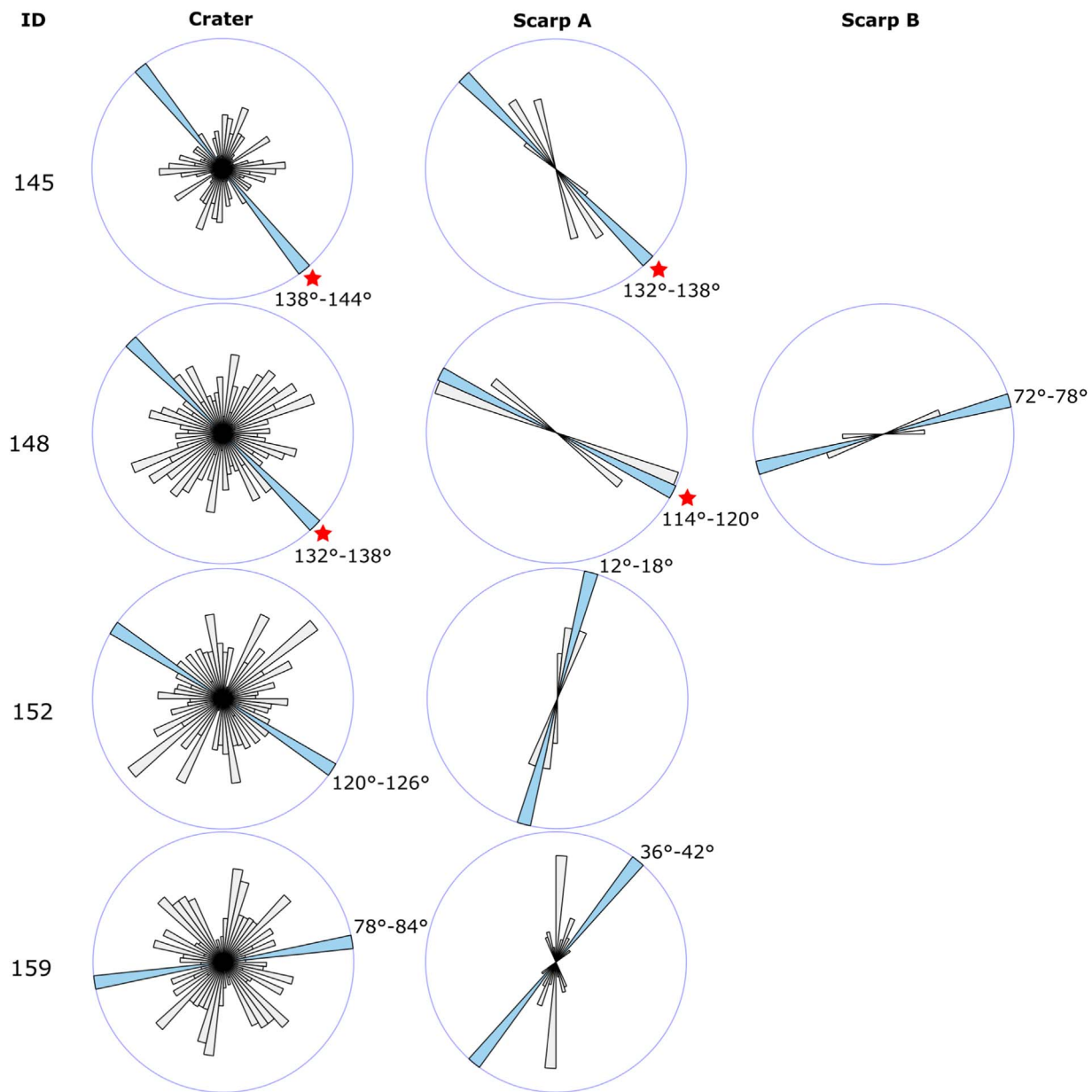


Figure A9. Rose diagrams showing the azimuth distributions of PIC rims and adjacent lobate scarps for craters 145–159 (Table A1). Modes are represented by blue petals, and red stars denote similar orientations between PIC straight rim segments and lobate scarps.

ORCID iDs

- Chloe B. Beddingfield <https://orcid.org/0000-0001-5048-6254>
 Kelsey Crane <https://orcid.org/0000-0001-5652-053X>
 Christian Klimczak <https://orcid.org/0000-0002-6811-8502>
 Richard Cartwright <https://orcid.org/0000-0002-6886-6009>

References

- Ahmadhadi, F., Daniel, J.-M., Azzizadeh, M., & Lacombe, O. 2008, *Tecto*, **27**, TC1016
 Anderson, E. 1951, The Dynamics of Faulting and Dyke Formation with Applications to Britain (New York: Hafner Publishing)
 Aittola, M., Öhman, T., Leitner, J., Kostama, V.-P., & Raitala, J. 2010, *Icar*, **205**, 356
 Aittola, M., Öhman, T., Leitner, J., et al. 2008, LPSC, **39**, 2137
 Aittola, M., Öhman, T., Leitner, J., & Raitala, J. 2007, *EM&P*, **101**, 41
 Anderson, J., Sides, S., Soltesz, D., Sucharski, T., & Becker, K. 2004, LPSC, **35**, 2039
 Banks, M. E., Xiao, Z., Watters, T. R., et al. 2015, *JGRE*, **120**, 1751
 Basilevsky, A., & Keller, H. 2006, *P&SS*, **54**, 808
 Beddingfield, C., Beyer, R., Cartwright, R., et al. 2020, LPSC, **51**, 1241
 Beddingfield, C. B., Burr, D. M., & Tran, L. T. 2016, *Icar*, **274**, 163
 Beddingfield, C. B., & Cartwright, R. J. 2020, *Icar*, **343**, 113687
 Belton, M., Chapman, C., Veverka, J., et al. 1994, *Sci*, **265**, 1543
 Binder, A. B., & McCarthy, D. W. 1972, *Sci*, **176**, 279
 Blair, D. M., Freed, A. M., Byrne, P. K., et al. 2013, *JGRE*, **118**, 47
 Burt, J. E., Barber, G. M., & Rigby, D. L. 2009, Elementary Statistics for Geographers (New York: Guilford Press)
 Byrne, P. 2018, *A&G*, **59**, 1.14
 Byrne, P. K., Klimczak, C., Celâl Şengör, A., et al. 2014, *NatGe*, **7**, 301
 Byrne, P. K., Klimczak, C., & Şengör, A. 2018, in Mercury. The View after MESSENGER, ed. S. C. Solomon, L. R. Ritter, & B. J. Anderson (Cambridge: Cambridge Univ. Press), 249
 Christensen, P., Engle, E., Anwar, S., et al. 2009, AGU FM, IN22A-06

- Cochrane, C. G., & Ghail, R. C. 2006, *JGRE*, **111**, E04007
- Collins, G. C., McKinnon, W. B., Moore, J. M., et al. 2009, in Planetary Tectonics, ed. T. R. Watters & R. A. Schultz (Cambridge: Cambridge Univ. Press), 264
- Cordell, B. M., & Strom, R. G. 1977, *PEPI*, **15**, 146
- Cosgrove, J. 2015, *GSLSP*, **421**, 41
- Crane, K. 2020, *Geomo*, **369**, 107366
- Crane, K. T., & Klimczak, C. 2017, *GeoRL*, **44**, 3082
- de Pater, J., & Lissauer, J. J. 2010, Planetary Sciences (Cambridge: Cambridge Univ. Press)
- Denevi, B., Seelos, F., Ernst, C., et al. 2016, *LPSC*, **47**, 1264
- Eckert, A., Connolly, P., & Liu, X. 2014, *GGG*, **15**, 4570
- Engelder, T., & Geiser, P. 1980, *JGR*, **85**, 6319
- Eppler, D. T., Ehrlich, R., Nummedal, D., & Schultz, P. H. 1983, *GSAB*, **94**, 274
- Fielder, G. 1961, *P&SS*, **8**, 1
- Fielder, G. 1965, Lunar Geology (London: Lutterworth Press)
- Fulmer, C. V., & Roberts, W. A. 1963, *Icar*, **2**, 452
- Galluzzi, V., Di Achille, G., Ferranti, L., Popa, C., & Palumbo, P. 2015, *GSLSP*, **401**, 313
- Galluzzi, V., Ferranti, L., Massironi, M., et al. 2019, *JGRE*, **124**, 2543
- Gault, D. E., Quaide, W. L., & Oberbeck, V. R. 1974, A Primer in Lunar Geology SEE N75-13730 04-91, *177*
- Gifford, A. W., & Maxwell, T. A. 1979, *LPSC*, **10**, 2597
- Harrison, J., & Falcon, N. 1934, *GeoM*, **71**, 529
- Harrison, J. V., & Falcon, N. L. 1936, *Quarterly Journal of the Geological Society*, **92**, 91
- Hartigan, J. A., & Hartigan, P. M. 1985, *The Annals of Statistics*, **13**, 70
- Hawkins, S. E., Boldt, J. D., Darlington, E. H., et al. 2007, *SSRV*, **131**, 247
- Helfenstein, P., Thomas, P., Veverka, J., et al. 2005, AAS/DPS Meeting, **37**, 36.01
- Herrick, R. R., Curran, L. L., & Baer, A. T. 2011, *Icar*, **215**, 452
- Herrick, R. R., & Forsberg-Taylor, N. K. 2003, *M&PS*, **38**, 1551
- Jaeger, J. C., Cook, N. G., & Zimmerman, R. 2009, Fundamentals of Rock Mechanics (New York: Wiley)
- Kinczyk, M. J., Prockter, L. M., Byrne, P. K., Susorney, H. C., & Chapman, C. R. 2020, *Icar*, **341**, 113637
- King, S. D. 2008, *NatGe*, **1**, 229
- Klimczak, C., Byrne, P. K., Şengör, A. C., & Solomon, S. C. 2019, *CaJES*, **56**, 1437
- Klimczak, C., Byrne, P. K., & Solomon, S. C. 2015, *E&PSL*, **416**, 82
- Kumar, P. S., & Kring, D. A. 2008, *JGRE*, **113**, E09009
- Maechler, M., & Ringach, D. 2013, Diptest: Hartigan's Dip Test Statistic for Unimodality Corrected Code. R package version 0.75-5
- Man, B., Rothery, D. A., Balme, M. R., Conway, S. J., & Wright, J. 2023, *NatGe*, **16**, 856
- Matsuyama, I., & Nimmo, F. 2009, *JGRE*, **114**, E01010
- McKinnon, W. B. 2014, *NatGe*, **7**, 251
- Melosh, H., & Dzurisin, D. 1978, *Icar*, **35**, 227
- Melosh, H., & McKinnon, W. 1988, Mercury (Tucson, AZ: Univ. Arizona Press), 374
- Melosh, H. J. 1976, *LPSC*, **7**, 2967
- Melosh, H. J. 1989, Impact Cratering: A Geologic Process (Oxford: Oxford Univ. Press)
- Morrison, G. 1984, Ontario Geological Survey Special Volume, 1, 513
- Murchie, S., Mick, A., Prockter, L., et al. 2016, MESSENGER MDIS CDR / RDR Software Interface Specification 1.2.23, JHUAPL
- Öhman, T. 2009, Res Terrae, Ser. A, **28**, 252
- Öhman, T., Aittola, M., Korteniemi, J., Kostama, V.-P., & Raitala, J. 2010, Large Meteorite Impacts and Planetary Evolution IV (McLean, VA: GSA), 51
- Öhman, T., Aittola, M., Kostama, V.-P., & Raitala, J. 2005, in Impact Tectonics, ed. C. Koeberl & H. Henkel (Berlin: Springer), **131**
- Öhman, T., Aittola, M., Kostama, V.-P., Hyvärinen, M., & Raitala, J. 2006, *M&PS*, **41**, 1163
- Öhman, T., Aittola, M., KOSTAMA, V.-P., Raitala, J., & Korteniemi, J. 2008, *M&PS*, **43**, 1605
- O'Keefe, J. D., & Ahrens, T. J. 1982, Geological Implications of Impacts of Large Asteroid and Comets on the Earth (McLean, VA: GSA), 103
- Osinski, G. R., & Pierazzo, E. 2013, Impact Cratering: Processes and Products (West Sussex, UK: Wiley-Blackwell), 1
- Pappalardo, R. T., & Collins, G. C. 2005, *JSG*, **27**, 827
- Perucca, L. P. A., Vargas, H. N., Rothis, L. M., Tapia Baldis, C. C., & Esper Angillieri, M. Y. 2016, *Journal of Iberian Geology*, **42**, 151
- Plescia, J. 1983, *Icar*, **56**, 255
- Poelchau, M., Kenkmann, T., & Kring, D. 2008, Large Meteorite Impacts and Planetary Evolution IV, **3073**
- Poelchau, M. H., Kenkmann, T., & Kring, D. A. 2009, *JGRE*, **114**, E01006
- Porco, C., Baker, E., Barbara, J., et al. 2005, *Sci*, **307**, 1237
- Price, N. J., & Cosgrove, J. W. 1990, Analysis of Geological Structures (Cambridge: Cambridge Univ. Press)
- Prockter, L., Thomas, P., Robinson, M., et al. 2002, *Icar*, **155**, 75
- Quaide, W. L., & Oberbeck, V. R. 1968, *JGR*, **73**, 5247
- Ramsay, J. G. 1967, Folding and Fracturing of Rock (New York: McGraw-Hill)
- Ramsey, J. 1968, Folding and Fracturing of Rock, Tech. Report (New York: McGraw-Hill)
- Reber, J., Schmalholz, S. M., & Burg, J.-P. 2010, *Tect*, **493**, 187
- Reimold, W. U., Brandt, D., & Koeberl, C. 1998, *Geo*, **26**, 543
- Robbins, S. J., & Riggs, J. D. 2023, *E&SS*, **10**, e2023EA002863
- Roddy, D. J. 1978, *LPSC*, **9**, 3891
- Ronca, L. B., & Salisbury, J. W. 1966, *Icar*, **5**, 130
- Schenk, P. M. 1991, *JGR*, **96**, 1887
- Schultz, P., & Gault, D. 1985a, *LPSC*, **16**, 742
- Schultz, P. H., & Gault, D. E. 1985b, *JGR*, **90**, 3701
- Schultz, P. H. 1976, Moon Morphology: Interpretations based on Lunar Orbiter Photography (Austin, TX: Univ. Texas Press)
- Shoemaker, E. 1963, Geological Society of America Centennial Field Guide-Rocky Mountain Section (Boulder, CO: GSA), 399
- Shoemaker, E. M. 1962, Physics and Astronomy of the Moon (New York: Academic Press), 283
- Shoemaker, E. M. 1977, in Meteorite Craters, Benchmark Papers in Geology, Vol. 36, ed. G. J. H. MacCall (Stroudsburg, PA: Hutchinson and Ross), **170**
- Singer, K. N., & McKinnon, W. B. 2011, *Icar*, **216**, 198
- Smith, B. A., Soderblom, L., Beebe, R., et al. 1981, *Sci*, **212**, 163
- Solomon, S. C. 1977, *PEPI*, **15**, 135
- Strom, R. G., & Sprague, A. L. 2003, Exploring Mercury (Chichester, UK: Springer)
- Strom, R. G., Trask, N. J., & Guest, J. E. 1975, *JGR*, **80**, 2478
- QGIS Development Team 2021, QGIS Geographic Information System (QGIS Association)
- Thomas, P., Veverka, J., Bell, J., III, et al. 1999, *Icar*, **140**, 17
- Thomas, P. G., & Allemand, P. 1993, *JGR*, **98**, 13097
- Tosi, N., Grott, M., Plesa, A.-C., & Breuer, D. 2013, *JGRE*, **118**, 2474
- Veverka, J., Thomas, P., Harch, A., et al. 1997, *Sci*, **278**, 2109
- Watters, T. R. 2021, *ComEE*, **2**, 9
- Watters, T. R., Cook, A., & Robinson, M. S. 2001, *P&SS*, **49**, 1523
- Watters, T. R., & Johnson, C. 2010, in Planetary Tectonics, ed. T. R. Watters & R. Schultz (Cambridge: Cambridge Univ. Press), **121**
- Watters, T. R., Murchie, S. L., Robinson, M. S., et al. 2009a, *E&PSL*, **285**, 309
- Watters, T. R., Solomon, S. C., Robinson, M. S., et al. 2009b, *E&PSL*, **285**, 283
- Watters, T. R., Robinson, M. S., Bina, C. R., & Spudis, P. D. 2004, *GeoRL*, **31**, L04701
- Watters, T. R., Robinson, M. S., & Cook, A. C. 1998, *Geo*, **26**, 991
- Watters, W. A. 2009, PhD thesis, MIT
- Watters, W. 2006, *LPSC*, **37**, 2163
- Weihns, G., Leitner, J., & Firneis, M. 2015, *P&SS*, **111**, 77
- Yazici, I., Cheng, H. C. J., Crane, K. T., & Klimczak, C. 2024, *JMaps*, **20**, 2308687
- Yazici, I., & Klimczak, C. 2021, *LPSC*, **52**, 1395
- Zeinhofer, M. F., & Barlow, N. G. 2021, *Icar*, **368**, 114586
- Zuber, M. T., Smith, D. E., Cheng, A. F., et al. 2000, *Sci*, **289**, 2097